



Nanoscale

Recent achievements toward the development of Ni-based layered oxide cathodes for fast-charging Li-ion batteries

Journal:	<i>Nanoscale</i>
Manuscript ID	NR-REV-10-2022-005701.R1
Article Type:	Review Article
Date Submitted by the Author:	15-Dec-2022
Complete List of Authors:	Zhang, Yuxuan; Purdue University, Engineering Technology; Materials Engineering Kim, Jae Chul; Stevens Institute of Technology, Song, Han Wook; KRISS Lee, Sunghwan; Purdue University, Engineering Technology; Materials Engineering

SCHOLARONE™
Manuscripts

Recent achievements toward the development of Ni-based layered oxide cathodes for fast-charging Li-ion batteries

Yuxuan Zhang¹, Jae Chul Kim², Han Wook Song³, and Sunghwan Lee^{1*}

¹ School of Engineering Technology, Purdue University, West Lafayette, IN 47907, USA

² Department of Chemical Engineering and Materials Science, Stevens Institute of Technology, Hoboken, NJ 07030, USA

³ Center for Mass and Related Quantities, Korea Research Institute of Standard and Science (KRISS), Daejeon 34113, South Korea

*Corresponding authors: sunghlee@purdue.edu

Abstract

The driving mileage of electric vehicles (EVs) has been substantially improved in recent years with the adoption of Ni-based layered oxide materials as the battery cathode. The average charging period of EVs is still time-consuming, compared to the short refueling time of an internal combustion engine vehicle. With the guidance from the United States Department of Energy, the charging time of refilling 60% of the battery capacity should be less than 6 mins for EVs, indicating the corresponding charging rate for the cathode materials is to be greater than 6 C. However, the sluggish kinetic condition and the insufficient thermal stability of the Ni-based layered oxide materials hinder further application in fast-charging operation. Most of the recent review articles regarding Ni-based layered oxide materials as cathode for lithium-ion batteries (LIBs) only touch degradation mechanisms under slow charging conditions. Of note, the fading mechanisms of the cathode materials for fast-charging, of which the importance abruptly increases due to the development of electric vehicles, may be significantly different from those of slow charging conditions. There are a few review articles regarding fast-charging, however, their perspectives are limited mostly to battery thermal management simulations, lacking experimental validations such as microscale structure degradations of Ni-based layered oxide cathode materials. In this review, a general and fundamental definition of fast-charging is discussed at first, then, we summarize the rate capability required in EVs and the electrochemical and kinetic properties of Ni-based layered oxide cathode materials. Next, the degradation mechanisms of LIBs leveraging Ni-based cathode under fast-charging operation are systematically discussed from electrode scale to particle scale and finally atom scale (lattice oxygen-level investigation). Then, various strategies to achieve higher rate capability, such as optimizing the synthesis process of cathode particles, fabricating single-crystalline particles, employing electrolyte additives, doping foreign ions, coating protective layers, and engineering the cathode architecture, are detailed. All these strategies need to be considered to enhance the electrochemical performance of Ni-based oxide cathode materials under fast-charging conditions.

1. Introduction

Innovation in transportation is key to stopping climate change. The Energy Information Administration reported that 37% of the total energy produced in the United States in 2021 was from petroleum sources.¹ A vast majority (91%) of these sources was consumed in the transportation end-user sector such as cars, trucks, and aircrafts. Indeed, the transportation sector is the largest contributor (28%) to U.S. greenhouse gas emissions, according to the Environmental Protection Agency, in 2021.² Reducing the petroleum reliance in transportation will, therefore, make a direct impact on immediately reduce the entire carbon footprint, shaping a sustainable future.

In light of this clear motivation, the transportation sector is getting electrified. For example, General Motors and Ford, the two largest car makers in the U.S., plan to end their production of engine-powered cars and trucks and will offer electric vehicles (EVs) exclusively by 2035.^{3,4} The key enabler of EVs is, undoubtedly, rechargeable batteries. Among many types of batteries, Li-ion batteries (LIBs) that adopt a lithium transition metal oxide (LiTMO₂) cathode govern the modern EV battery technology with their high energy density and good round-trip efficiency.⁵⁻⁷

As the market for EVs is expanding rapidly, the need for high-performance batteries continues to grow.^{8,9} To enable high energy density, research efforts to design transition metal compositions for the layered oxide cathode have centered on implementing nickel as a redox center. Ni-based layered oxides such as LiNi_xCo_yMn_zO₂ (NCM, $x + y + z = 1$) and LiNi_xCo_yAl_zO₂ (NCA, $x + y + z = 1$) have been gradually replacing LiCoO₂.¹⁰⁻¹² In order to meet the energy density goal of 350 Wh kg⁻¹ and 750 Wh L⁻¹ at the cell level, as established by the U.S. Department of Energy (DOE) and U.S. Advanced Battery Consortium (USABC),¹³ Ni-based layered oxides with high Ni-content (Ni ≥ 80%) are considered suitable for EV applications due to the high specific capacities (200–250 mAh g⁻¹), high working voltage (3.6–3.8 V) and relatively low cost.^{14, 15} The driving mileage of EVs that adopt these Ni-rich cathodes has been substantially improved, compatible to that of the internal combustion engine vehicles (ICEVs), increasing the market penetration of EVs.¹⁶

However, the average charging time required for EVs (recharging 80% of its capacity in about 1 h) is incompatible to the short refueling time of ICEVs (refueling can be done in less than 10 mins).¹⁷⁻¹⁹ According to the recent guidelines of fast-charging released by the U.S. DOE, the ultimate goal for fast-charging is to refill 60% of the full battery capacity in 6 min or less, which indicates that the charging rate for the battery is greater than 6C.²⁰ In general, the fast-charging capability of LIBs is limited by mechanical and electrochemical properties of Ni-based layered oxide cathodes.^{21, 22} First, the structural instability of highly oxidized Ni-based layered oxides makes them hard to accommodate rapid volume change upon fast-charging.^{23, 24} This results in micro-cracks generated throughout the secondary particle of Ni-based cathodes, creating excess surface areas that facilitate the formation of cathode-electrolyte interphases.^{25, 26} Second, poor charge transport kinetics of Ni-based layered oxides can induce high cell impedance.^{27, 28} Especially for the polycrystalline Ni-based layered oxides materials, low electronic and ionic conductivities of the primary crystals can limit the rate capability.^{29, 30} Consequently, the Ni-based layered oxide cathodes can degrade faster at fast charging (e.g., 6C) than at slow charging (e.g., 0.5C).³¹⁻

In this review, we highlight recent progresses in the development of Ni-based LiTMO_2 for EV applications. We will first define fast-charging, discuss rate capability practically required in EVs, and summarize the electrochemical and kinetic properties of Ni-based layered oxide cathode materials. Then, a comprehensive discussion of the major degradation mechanisms of Ni-based layered oxide cathode materials under fast charging conditions will follow. The state-of-the-art approaches to address cathode degradation and enhance the rate performance of Ni-based layered oxide will be discussed. Finally, an outlook on future directions of designing Ni-based layered cathode for LIBs for superior fast-charging performance will be presented.

2. Features of Fast-charging and Ni-based oxide cathode materials

2.1 The definition of fast-charging

Technologies to enable fast-charge or extreme fast-charge (XFC) to recharge batteries in a few minutes have drawn extensive research interest and exhibited a great market prospect. A comparison, available in the literature,³⁴ of 525-mile intercity travel from Salt Lake City, Utah to Denver, Colorado between internal combustion engine vehicles (ICEVs) and battery electric vehicles (BEVs) is illustrated in Fig. 1A. As the baseline for the comparison, it takes 8 h and 23 min for the ICEV to travel 525 miles with one 15-min refueling stop. For the 300-mile-range BEV, it takes 9 h and 16 min to cover the same distance, 53 mins more than ICEV, due to a recharging time of 68 mins at 120 kW. In the case of a 200-mile-range BEV equipped with 400 kW XFC, the total travel time is 8 h and 46 mins, 30 mins less than the 300-mile BEV, even with two recharge stops. Furthermore, the estimated travel time of the 300-mile BEV with 400 kW XFC is 8 h and 31 mins, which is only 1.6% longer than the ICEV, with one recharge stop of 23 mins at 275 miles. To finish the recharge in 23 mins to go for another 250 miles, the charging speed should be faster than 11 miles min^{-1} . Of note, the fast-charging goal set by the U.S. DOE is 20 miles min^{-1} on average or recharging up to 80% of the battery capacity in 10 mins or less.³⁵ However, the charging speed of most of the BEVs (e.g., Mitsubishi i-MiEV,³⁶ Nissan Leaf,³⁷ BMW i3,³⁸ and Chevy Bolt³⁹) remains below 3 miles min^{-1} as indicated in Fig. 1B. Tesla Model S has achieved a charging rate 5.6 miles min^{-1} with its state-of-the-art 120 kW supercharger,^{40, 41} but this charging speed still does not meet the fast-charging requirement proposed by DOE. Thus far, the typical charging rate demonstrated practically is in the ballpark of 2C or even less,^{34, 42} corresponding to a charge with a power of 50 kW for most BEVs as well as 120 kW for Tesla.^{20, 42} The higher charging speed may require the voltage rating of BEV from 400 to 1000 V that increases the charging rate from 1.5 to 6 C for the battery as exhibited in Table 1.²⁰

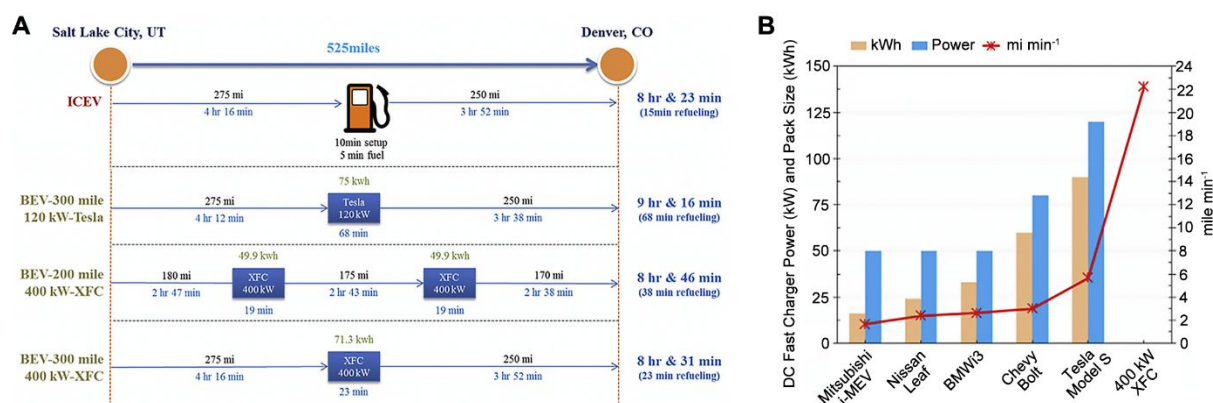


Fig. 1. (A) Comparison of an intercity travel from Salt Lake City to Denver.³⁴ (B) Charging profiles for BEVs with direct-current fast-charging capabilities in the market.³⁵

Charger Voltage	400-1000V		
Charge Inlet	XFC Designed Inlet (s) for 1000V @400A		
Vehicle	600V, 400A, 240kW	800V, 400A, 320kW	1000V, 400A, 400kW
	1000V, 210-280A, 210-280kW		
Battery	2.0-3.3C	3.3-4.6C	4.6-6C

Table 1. Timeline of BEVs and battery C-rate to support XFC.³⁴

2.2 The electrochemical property of Ni-based layered oxide materials

LiNiO₂ that is isostructural to LiCoO₂ was investigated as a cathode material to increase energy density and lower materials cost for LIBs.^{26, 43-46} However, LiNiO₂ destabilizes upon delithiation at high voltage, undergoing irreversible phase transformations involving O₂ release.⁴⁶⁻⁴⁸ To improve electrochemical stability of LiNiO₂, Co,⁴⁸⁻⁵⁰ Mn,^{44, 51, 52} and Al⁵³⁻⁵⁵ were incorporated into LiNiO₂.⁵⁶ It has now proven that Al³⁺ and Mn⁴⁺ do not participate in the redox process but enhance the structure and thermal stability of the material. Co³⁺ contributes to stabilizing the layered structure, improving the rate capability of the layered oxide cathodes.⁵⁷⁻⁵⁹ Many studies confirmed that the high Ni content will lead to a concomitant increase in specific capacity at the expense of the electrode stability as indicated in Fig. 2A.⁵⁹⁻⁶² This trade-off effect of high Ni content in the cathode can be understood by the increased high-valence state Ni ions (i.e., Ni⁴⁺) that readily react with the electrolyte, although these high valence state Ni ions benefit the specific capacity of the cathode.⁶³⁻⁶⁶

According to the in situ XRD measurement (not shown) of various Ni-based oxide cathode materials, the c-lattice parameter varies substantially with the cathode composition.⁶⁷ The c-lattice parameter in Fig. 2B decreases substantially at high voltage as the Ni fraction increased. The variation of the lattice parameters results from complex phase transitions upon Li extraction.⁶⁷ As shown by the dQ/dV-plots in Fig. 2C-F, NCM materials undergo different phase transitions with the different Ni content. Upon charge, all NCMs phase-transform from hexagonal (H1) to monoclinic (M) at ~3.7 V. Ni-rich (80% or more) NCM cathodes show additional phase transition, M-to-hexagonal (H2) at ~4.0 V and H2-to-hexagonal (H3) phases at ~4.2 V. The H2-to-H3 transition is more evident in LiNi_{0.95}Co_{0.025}Mn_{0.025}O₂ at lower voltage than in LiNi_{0.8}Co_{0.1}Mn_{0.1}O₂. No significant H2-H3 transition is observed in LiNi_{0.6}Co_{0.2}Mn_{0.2}O₂ as it requires 4.6 V, which is higher than the charge cutoff voltage. Here, it should be emphasized that the shrinkage of the c-lattice parameter mainly originates from the H2-H3 transition

at high voltage, leading to substantial volume change of NCM.^{68, 69} Thus, electrochemical and mechanical stability of Ni-rich NCM largely depend on their high-voltage characteristics.⁷⁰⁻⁷²

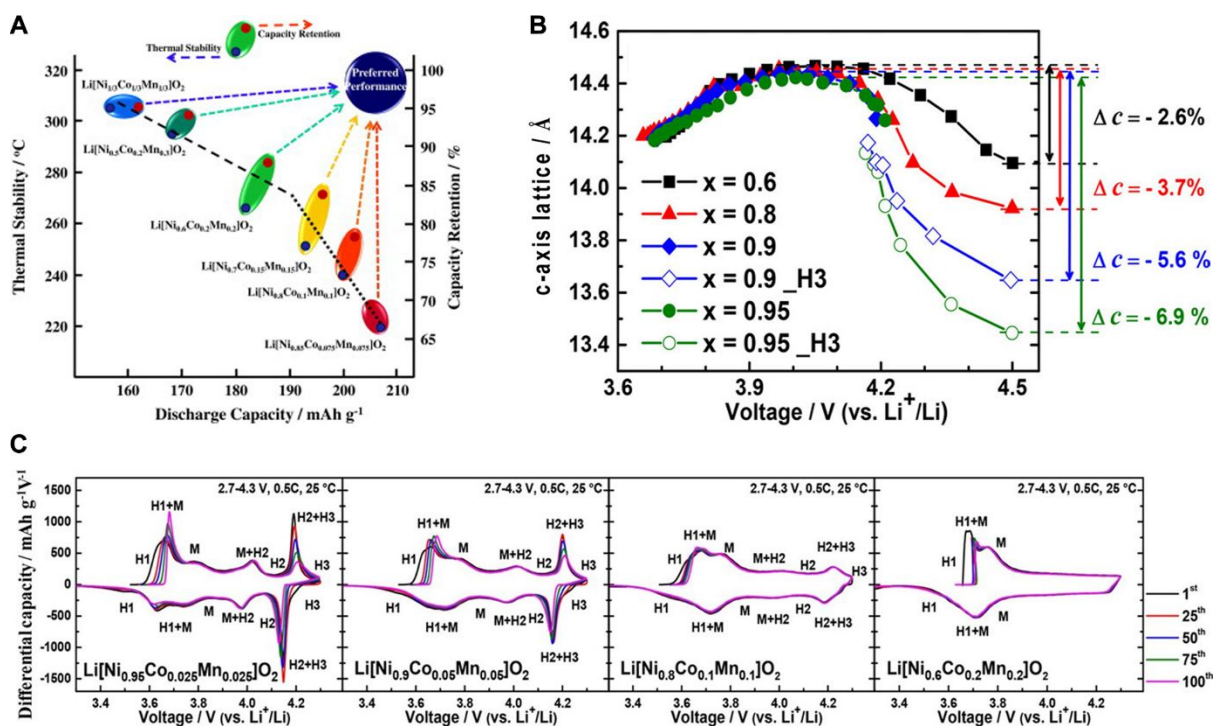


Fig. 2. (A) A map summarizing the trend relationship between discharge capacity, thermal stability, and capacity retention of NCM materials.⁶⁰ (B) c-axis lattice parameter of Ni-rich materials as a function of the cell voltage where x indicates the content of Ni in NCM.⁶⁷ (C)-(F) dQ/dV profiles of Ni-rich materials as a function of the number of cycles, ranging the Ni content from 0.6 to 0.95.⁶⁷

2.3 The kinetic property of Ni-based layered oxide materials

It is critical to understand the kinetic property of Ni-based layered oxide materials to further optimize the rate performance. Typically, the transport of Li ions within Ni-based layered oxide materials can be categorized into several mechanisms: diffusion in bulk, diffusion across the grain boundaries, and diffusion along the grain planes. For bulk diffusion, there are two Li-ion transport pathways in the layered structure.^{73, 74} Li-ion diffuses from one octahedral site to the next octahedral site through an intermediate-tetrahedral site (Fig. 3A) or an oxygen dumbbell (Fig. 3B). Specifically, Li-ions prefer to migrate through oxygen dumbbell hopping at the initial of the charging process. Then, when more than 1/3 Li-ions were extracted from the cathode, the tetrahedral site hopping becomes a dominant role in Li-ion transport.⁷⁴ The activation energy for Li-ions transport in the suggested pathways is closely associated with the volume of Li-O tetrahedrons and octahedrons in the Li slab.^{73, 75} In Fig. 3C, the stacking of Li slabs and transition metal (TM) slabs alternates, and d_1 and d_2 are the height of the TM and Li slabs, respectively. As a result, the large Li-ion diffusivity with low activation energy along the diffusion pathway is largely ascribed to the large Li slab spacing. Meanwhile, Li ions can also diffuse along with the grain planes and across the planes, as indicated in Fig. 3D.⁷⁶ Grain boundaries with specific orientations such as $\Sigma 2(110\bar{4})$ and $\Sigma 3(\bar{1}10\bar{2})$ and hence different microstructures regulate Li migration in different ways, which leads to different Li diffusivities and overall conductivities.⁷⁶ In most cases, Li-ion diffusion at grain boundaries can be facilitated, compared to that in the bulk due to the

kinetically favorable Li-ion transport environment (i.e., reduced energy barrier for migration) at/near the grain boundaries.^{77, 78} The thicker disordered phases at/near the grain boundaries of NCM cathode materials generally leads to 10 times higher Li transport than that in bulk.⁷⁶

In addition, the state of charge (SoC) of the NCM cathode dictates Li kinetics.⁷⁹ As shown in Fig. 3E, in the beginning of the charging process, D_{Li^+} gradually increases from 10^{-9} $\text{cm}^2 \text{s}^{-1}$ and reaches 10^{-8} $\text{cm}^2 \text{s}^{-1}$ at $\text{Li} = 0.5$ upon delithiation. Then it decreases back to 10^{-9} $\text{cm}^2 \text{s}^{-1}$ at $\text{Li} = 0.1$. At the end of charging, D_{Li^+} rapidly decreases to 10^{-10} $\text{cm}^2 \text{s}^{-1}$. The sluggish Li kinetics at the initial SoC of the cathode are mainly ascribed to the H1 phase that contains the high Li content with a few Li vacancies and the narrow Li slab spacing.^{29, 79} As charging continues, the new Li vacancies are generated and the spacing of Li slabs gradually increases, facilitating Li diffusion. At the end of charge, the transition metal ions are in the highest valence state, which attracts the electron cloud from oxygen and decreases the O-O repulsion, leading to the sharp volume decrease of the unit cell.⁷⁹ Thus, D_{Li^+} is generally small at the initial of the charging process and at the overcharging state. Upon discharge, D_{Li^+} remains high at $10^{-7} - 10^{-8}$ $\text{cm}^2 \text{s}^{-1}$ and decreases to 10^{-11} $\text{cm}^2 \text{s}^{-1}$ at the end of discharge. High D_{Li^+} in the beginning of discharge reflects high concentration gradient across the cathode-electrolyte interface, and sluggish diffusion at the end of discharge results from Li redistribution in the bulk, as commonly observed in Li cathodes.^{80, 81}

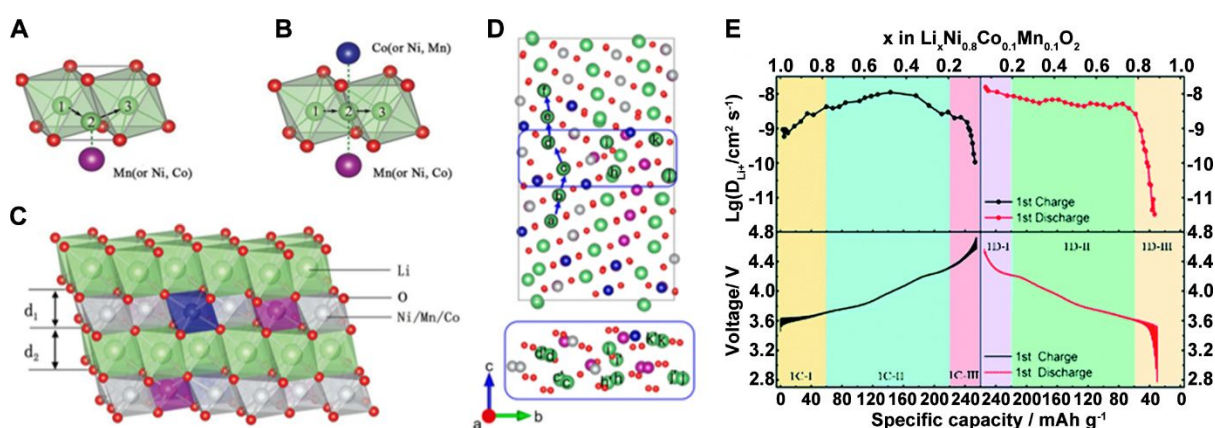


Fig. 3 (A) Tetrahedral site pathway and (B) oxygen dumbbell pathway for Li-ion diffusion in NCM layered structure.⁷⁴ (C) The lattice of NCM layered structure.⁷⁴ (D) Li diffusion across (top) and within (bottom) the grain boundary plane.⁷⁶ (e) First cycle GITT curves (bottom) and the corresponding D_{Li^+} (top) of NCM811.⁷⁹

3. Degradation mechanism under fast-charging

Charging batteries in a shorter time inevitably requires higher current density than the usual. Therefore, batteries at fast charge are under abusing conditions that likely accelerate their degradation. Indeed, degradation of the Ni-based layered oxide cathodes is a critical obstacle to achieving capacity retention (i.e., long cycle life) for practical applications.⁸²⁻⁸⁴ This section discusses the effect of Li transport kinetics and surface oxygen loss to further understand the degradation mechanisms of Ni-based layered oxide cathodes.⁸⁵⁻⁸⁷

3.1 Kinetic inhomogeneity in multi-scale

3.1.1 Inhomogeneity in the electrode-scale

The LIB cathode consists of multiple components (i.e., the active material, carbon additive, and binder), which need to be coherently interoperated to obtain desirable battery performance. The complex, heterogeneous construction makes it difficult to probe the cathode in various length- and time-scales. The morphological and chemical characteristics of Ni-based layered oxide at the microscale have been recently investigated by Yang et al.⁸⁸ They leveraged hard X-ray phase-contrast nanotomography to compare morphology of more than 600 particles in the NCM622 cathode cycled 10 times with a 5C rate (Fig. 4A). Three representative particles were marked in red, green, and blue, as shown in Fig. 5A, corresponding to the severely damaged, mildly damaged, and least damaged particles, respectively. The coexistence of differently damaged particles implies the inhomogeneity of the NCM particles in the cathode. They also observed that particles located near the separator are likely damaged more than those near the current collector, as illustrated in Fig. 4B. Li et al.⁸⁹ monitored the dynamic evolution of the chemical and morphological characteristics of thousands of individual NCM particles through nanoholotomography at different cycles and SoCs. In Fig. 4C, the concentration of severely damaged particles (marked in red) increases, while the distance of neighboring particles considerably reduces, as the cycle number increases from 10 to 50. These variations likely disintegrate and distort the cathode due to different mechanical properties of the NCM particles (elastic modulus, $E \sim 140$ GPa) and carbon/binder domains ($E \sim 2$ GPa).⁸⁹ The transport of Li ions and electrons across the interfaces between active materials and carbon/binder domain can be disrupted, leading to poor percolation of charge transport pathways. Mistry et al.⁹⁰ indicated the inhomogeneous electrode would lead to the preferential intercalation of the NCM materials, which may induce detrimental heat spots in the electrode and trigger safety issues (e.g., fire or explosion) of the entire cell.⁹⁰

To explain the electrode level inhomogeneity and understand the degradation mechanisms at fast charge, Park et al.⁹¹ exploited autocatalytic and autoinhibitory reactions to prepare NCM particles with compositional variation. Fig. 4D shows the Li content in the cathode particles at two different rates. They found that many particles remain lithiated at 2C unlike uniform delithiation observed at 0.05C. This rate-dependency is attributed to different Li kinetics of NCM particles with different compositions, leading to inhomogeneous Li distribution (i.e., non-uniform SoC) over multiple particles upon galvanostatic delithiation.⁹¹ This can polarize the cell substantially, limiting capacity at charge cutoff voltage.

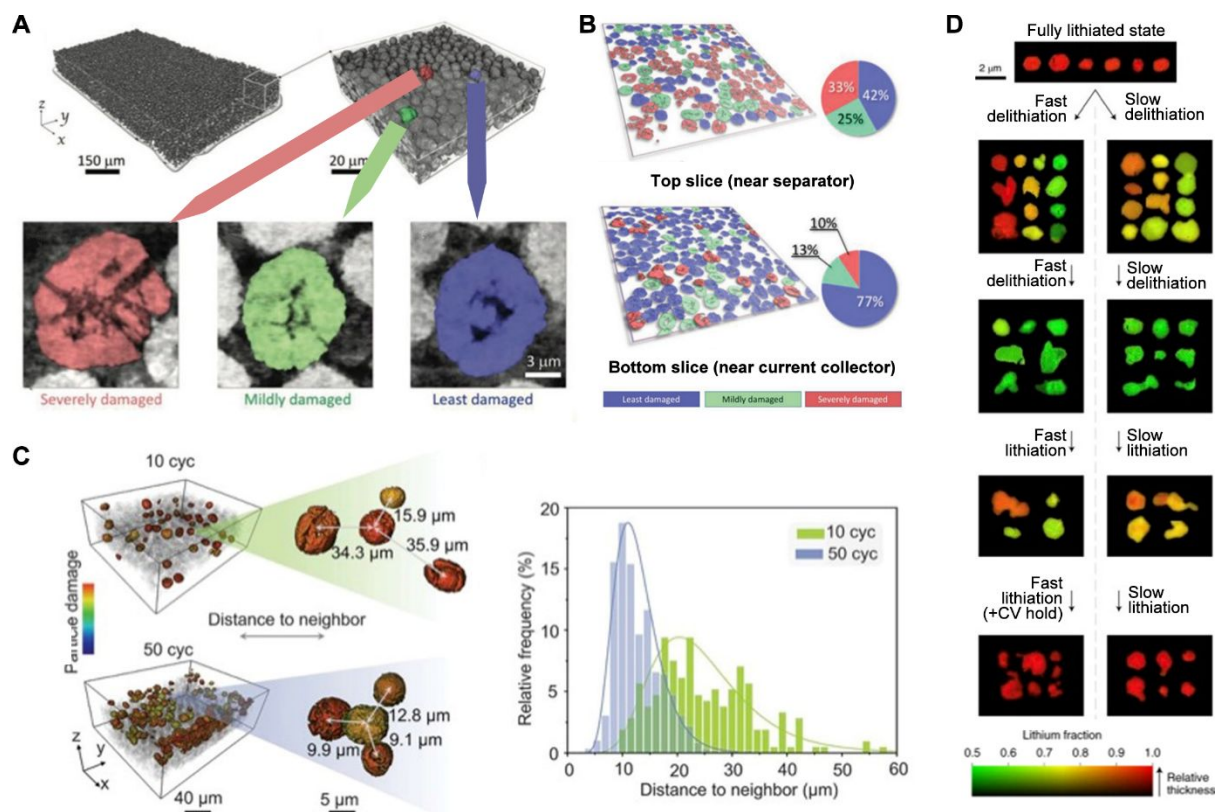


Fig. 4. (A) 3D rendering of micro-/nanotomography images of an NCM electrode and three of the representative particles highlighted in red, green, and blue, indicating severely damaged, mildly damaged, and least damaged particles, respectively.⁸⁸ (B) Slices over two particle layers that are close to the ten-cycled electrode's top surface (near the separator) and the aluminum current collector (bottom of the ten-cycled electrode).⁸⁸ (C) The spatial distributions of the severely damaged particles measured by nano-holotomography in the 10-cycled and 50-cycled electrodes and the probability distributions of the distance between two neighboring severely damaged particles in 10-cycled and 50-cycled electrodes.⁸⁹ (D) Particles sampled from fast-cycled (2C) cells and slow-cycled (0.05C) cells during the second cycle at states-of-charge corresponding to average lithium fractions of 0.75 → 0.50 → 0.75 → 1.00, respectively.⁹¹

3.1.2 Inhomogeneity in the particle-scale

In addition to the inhomogeneity at the electrode level, the heterogeneous distribution of the charge in a single particle is observed. Chueh and coworkers used a synchrotron-based transmission X-ray study to show depth-dependent SoC in a secondary particle and found more than 10% variation of Li concentration within the particle.⁹² This uneven charging of the secondary particle is attributed to the anisotropic volume change of the primary particles.⁹² In addition, the higher current density may intensify the local inhomogeneity of charge distribution and chemical environment (e.g., valence state of transition metals) over a secondary particle. Xu et al.⁹³ suggested two types of inhomogeneous charge distribution (rod- and gravel-like) in NCM particles, as shown in Fig. 5A. Both rod- (upper) and gravel-like (bottom) NCM particles show more oxidation in surface regions than in bulk due to the greater electrical and ionic conductivity near the surface. In addition, they specified the spatial distribution of Ni oxidation states in both NCM particle models. Rod-type NCM shows linear, parallel configuration of oxidized Ni, while gravel-NCM has a random arrangement of the 2D nanodomain valence gradient

vectors. The two distinct Ni valence patterns correspond to different crystalline orientations that determine the redox reaction pathway and charge distribution in the secondary particle. This inhomogeneity at the particle-scale illustrates that the overcharged regions in a particle are susceptible for the oxygen loss at a high SoC, which will be discussed later.

In order to further investigate the morphology degradation of the particle in terms of the charging rate, Xia et al.⁹⁴ depicted the 3D rendering of the particle through X-ray micro/nano tomography before and after 50 cycles under different rates (0.5C, 1C, 2C, 5C, 10C) In Fig. 5B, 2D virtual cross-sectional images at the center of the particles exhibit morphological defects. The degree of particle fracture observed is proportional to the charge rate. The particle fracture can be ascribed to the oxygen loss from the unstable H3 phase due to the partially overcharged region in the cathode. The detailed mechanism of oxygen loss and related capacity degradation will be provided in the following section (3.2). They also demonstrated that large secondary particles have low tolerance against crack formation compared with small particles at fast charge. Generally, crack formation of cathode particles at a high rate is irreversible, one of the main reasons for the capacity fade upon fast-charging.⁹⁵⁻⁹⁷ Through the combination of machine learning and high-resolution hard X-ray nano-tomography, Jiang et al.⁹⁸ found the detachment of inactive materials (i.e., additives and binders) from NCM particles in the cathode. Fig. 5C shows a reconstructed 3D model that reflects the physical contact between the NCM particle and surrounding conductive carbon/binder domain matrix. The detachment of the active NCM particles from the carbon/binder domain was observed at the particle level and marked as blue void regions. This results from uneven anisotropic volume change during repetitive charge-discharge processes, increasing impedance across the surface of the NCM particle.

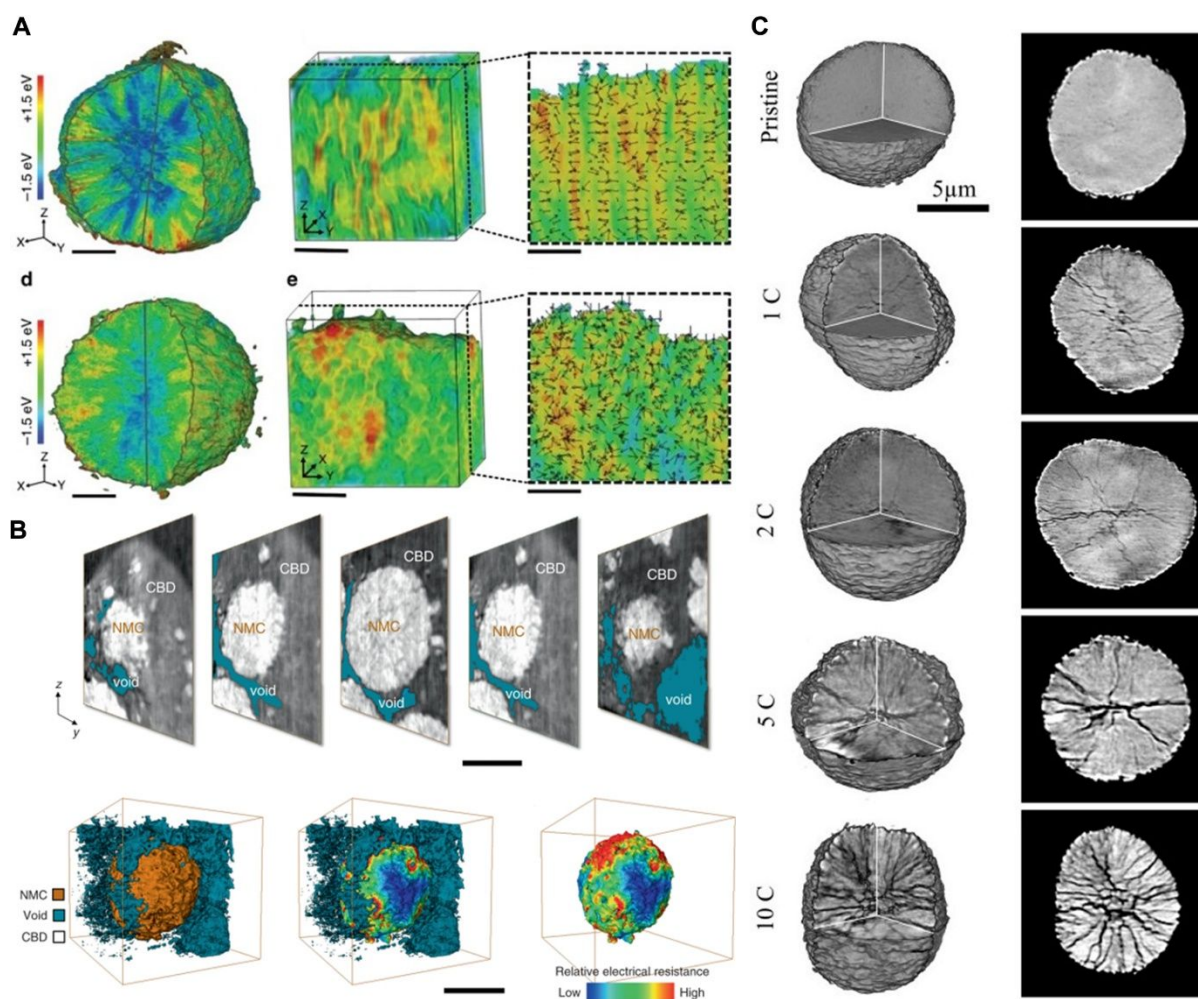


Fig. 5. (A) 3D Ni valence state distribution, and 2D nanodomain valence gradient of the rod-NCM and gravel-NCM.⁹³ (B) The 3D rendering of the particles at the pristine state and after 50 cycles at 1 C, 2 C, 5 C, and 10 C, and the corresponding 2D virtual slices of the particles.⁹⁴ (C) The 3D rendering of the segmentation results and the calculated charge distribution over two regions of interest with the carbon/binder domain set to be transparent for better visualization of the NCM particle (orange) and the voids (gray-blue).⁹⁸

3.2 Oxygen loss due to thermodynamic instability

It has been broadly reported that high-voltage instability of the H3 phase of NCM leads to unfavorable oxygen evolution, transition metal dissolution, and irreversible phase transformation (Fig. 6A).^{68, 99, 100} Charge compensation at high voltage can involve not only transition metal redox but also oxygen redox. Especially, oxidized Ni^{4+} in the NiO_6 octahedra can be stabilized by oxidizing surrounding oxygen. The increasing amount of overcharged (at high SoC) particles/regions with high current density, as discussed above, is thus susceptible for severe oxygen loss in the Ni-based layered oxide cathode. At high voltage, lattice oxygen may have several forms, including singlet oxygen ($^1\text{O}_2$), peroxide anodic radicals (O-O^\cdot), and peroxide bonds between transition metal ions (MO-OM), all of which have been experimentally identified.^{68, 101-103}

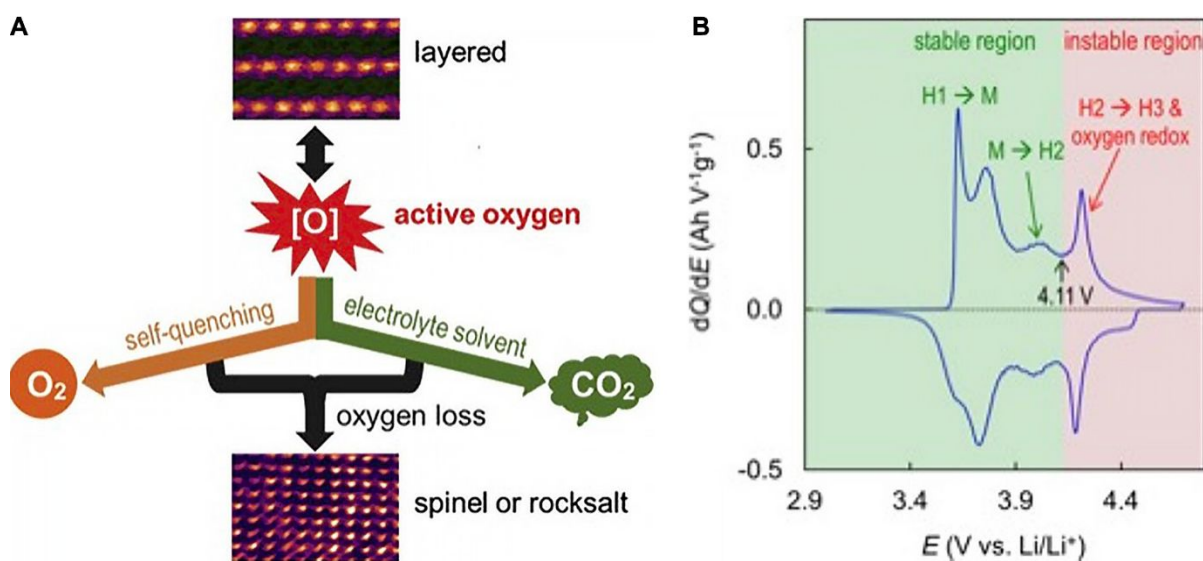


Fig. 6. (A) Schematic illustration of oxygen loss and the related effects.⁶⁸ (B) Correlation of oxygen evolution with SoC, potential, and differential capacity of NCM811 cathode, where the pink shaded area corresponds to the H2→H3 transition region while the green area indicates stable region of H1 and H2.⁶⁸

3.2.1 Phase transformation

Phase transitions from layered to spinel and from spinel to rock-salt result from oxygen loss. These transitions become evident with large delithiation.⁸⁶ Oxygen evolved from the cathode oxidizes the electrolyte, forming carbon dioxide (CO₂) exothermically, the sign of battery failure. The effect of the gas generation on battery degradation will be detailed in section 3.2.2. Layered NiO₂ (Fig. 7A) at a highly delithiated state can transform to spinel Ni₃O₄ (Fig. 7B) by oxygen loss with the formation of active oxygen intermediates.¹⁴ Oxygen vacancies formed by oxygen loss at high voltage could significantly decrease a Ni migration barrier to the adjacent, empty Li site (Fig. 7C), leading to the Ni/Li intermixing. This eventually alters the surface structure from the layered to the rock-salt (Fig. 7D).¹⁴ Without exception, the oxygen evolution reaction for all Ni-based layered oxides in the cathode was observed near the start of the H2 to the H3 phase transition, corresponding to the 75-80% SoC. Generally, these active oxygen intermediates can react with the electrolyte immediately. Also, the spinel and rock-salt phases are localized near the surface of NCM particles.¹⁰⁴ According to electron energy-loss spectroscopy (EELS), Yang et al.⁸⁶ argued that the phase transition can further extend to the bulk of NCM particles as a result of fast charging. In Fig. 7E, the O pre K-edge peak completely disappears deep in the particle (~30 nm) at a high rate. High-resolution transition electron microscopy (HRTEM) in Fig. 7F shows that the thick rock-salt phase was indeed formed on NCM811. This irreversible phase transformation can generate local stress along grain boundaries.^{105, 106} The stress concentration may accelerate the particle fracture. As the fractured surface of the NCM particle allows the liquid electrolyte to infiltrate, the newly exposed surface also undergoes the irreversible phase transitions associated with oxygen loss.¹⁰⁷

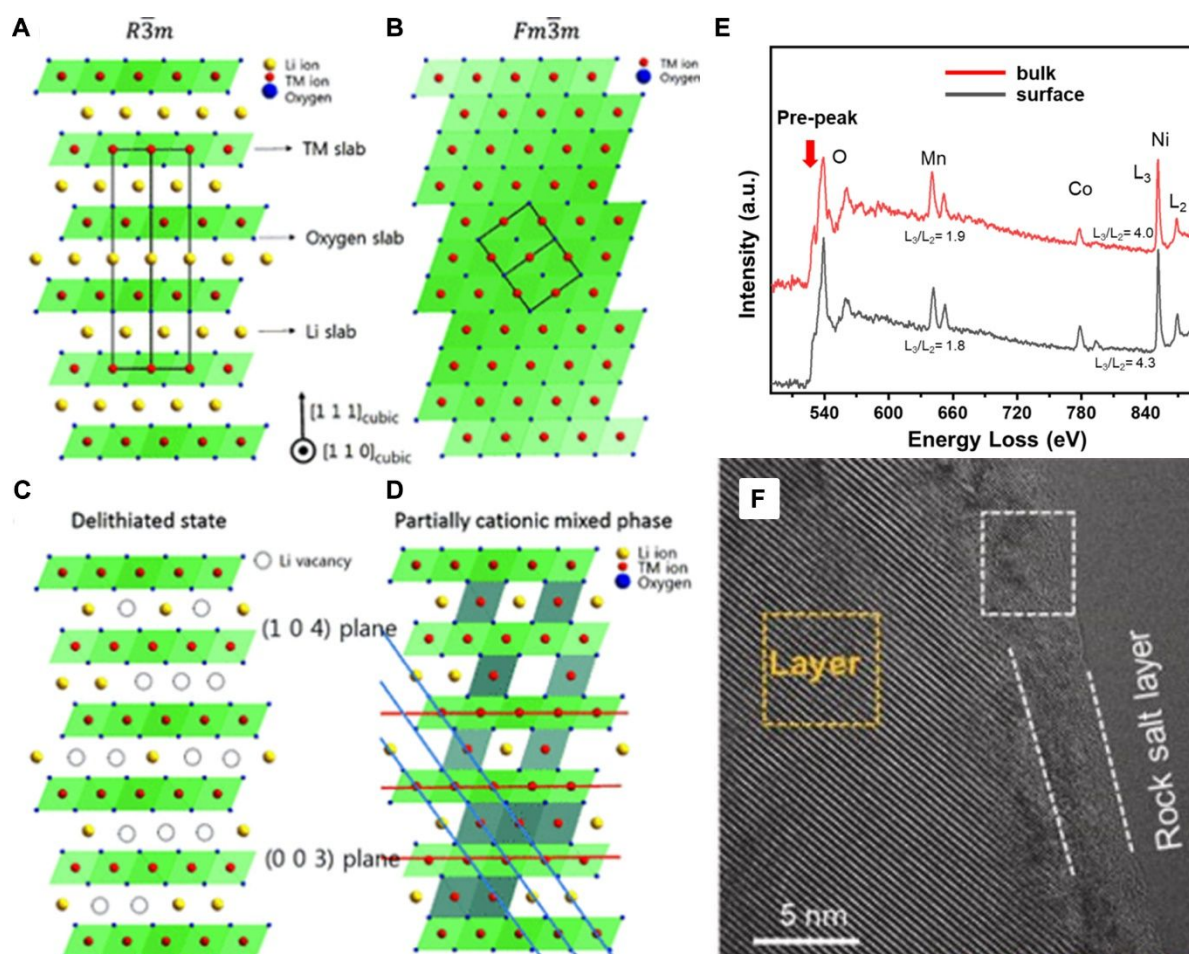


Fig. 7. Schematic diagram of ordered and disordered phases and their structural transitions in layered lithium metal oxides. (A) Ordered $R\bar{3}m$ structure, (B) Cation mixing phase with $Fm\bar{3}m$ structure, (C) $R\bar{3}m$ structure with Li vacancies at a highly charged state and (D) Cation mixed phase with partial TM ions in Li layer.¹⁴ (E) EELS (F) HR-TEM images of high-loading NCM811.⁸⁶

3.2.2 Gas release

Gas release from the Ni-based layered oxide cathode is one of the main causes of the thermal runaway of Li-ion batteries. The generated gaseous products mainly consist of O_2 , CO_2 , and CO (Fig. 8A).¹⁰⁸ As discussed previously, fast-charging can develop non-uniformity of Li composition from a particle to an electrode level, leading to local overcharge in the NCM cathode. According to electrochemical reaction pathways described in Fig. 8A, oxidized ethylene carbonate (EC) can generate CO (and/or CO_2) and protic species ($R-H^+$) and release electrons at the particle/electrolyte interface upon charging when cell voltage is higher than the electrochemical stability limit of the carbonate electrolyte. To maintain charge balance, Li ions should be extracted from the electrolyte and reinserted into the Ni-based layered oxide cathode. This self-discharge reaction at overcharge substantially decreases the Coulombic efficiency of the cell.

The gas generation from the charged NCM811 cathode was investigated by differential electrochemical mass spectrometry (DEMS).¹⁰⁸ In Fig. 8B, O_2 , CO_2 and CO generation corresponds to the H2-H3 phase transition at ~ 4.2 V. Oxygen oxidation in the overcharged H3 phase at high rates leads to oxygen gas evolution that reduces Ni,¹⁰⁹ forming the surficial spinel and/or rock-salt structures as discussed in

section (3.2.1). Note that overcharged regions in the cathode may release oxygen and generate CO, CO₂ and H₂O chemically (Fig. 8A). H₂O generated can accelerate transition metal dissolution from Ni-based layered oxide (see Section 3.2.3).

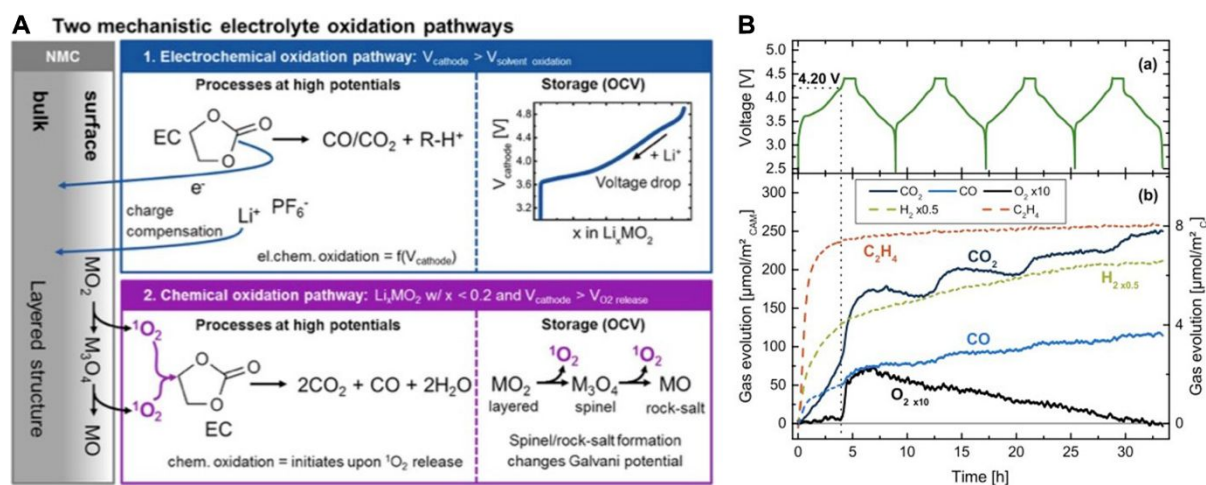
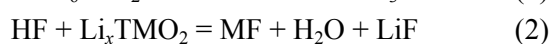


Fig. 8. (A) Schematic description of the proposed electrochemical and chemical electrolyte oxidation pathways occurred at high potentials.¹⁰⁸ (B) Cell voltage vs. time of an NCM811-Graphite cell over four charge/discharge cycles and evolution of CO₂ (dark blue), H₂ (green), C₂H₄ (orange), CO (blue), and O₂ (black, 10-fold magnified) as a function of time.¹⁰⁸

3.2.3 Transition metal dissolution

Owing to the harsh condition of fast-charging, the erratic H3 phase can be accumulated in the cathode. It is generally accepted that the transition metal ions dissolution accelerated by H₂O generation would result in capacity fading due to the deficiency of the Li-ion insertion sites in Ni-based particles.¹¹⁰⁻¹¹² H₂O can hydrolyze LiPF₆ in the electrolyte, producing HF that continuously corrodes cathode surface. This corrosion process is described as follows:



The dissolved transition metal ions further migrate to the anode and will be reduced to metal that make the solid-electrolyte interphase (SEI) electronically conductive. As the anode cannot be fully passivated, SEIs will continuously grow upon repetitive charge and discharge, depleting Li ions and electrolyte molecules. The cathode/anode ratio would be altered by the Li ions loss due to the extracted Li ions being unable to intercalate into the anode, which leads to the overcharging of the cathode. Ko et al.¹¹³ investigated how the transition metal composition of a Ni-rich NCM particle changes over cycles through EDS mapping. Compared to pristine NCM in Fig. 10A, the transition metal content decreases as the cycle number increases in Figs. 9B and C. Notably, the transition metal ions are more likely released from the cracked NCM particle. Using operando X-ray absorption spectroscopy, Jung et al.¹¹⁴ found that increasing transition metal concentration at the graphite anode when the NCM622 cathode was cycled at > 4.5 V, associated with the H3 phase formation, in Fig. 9D.

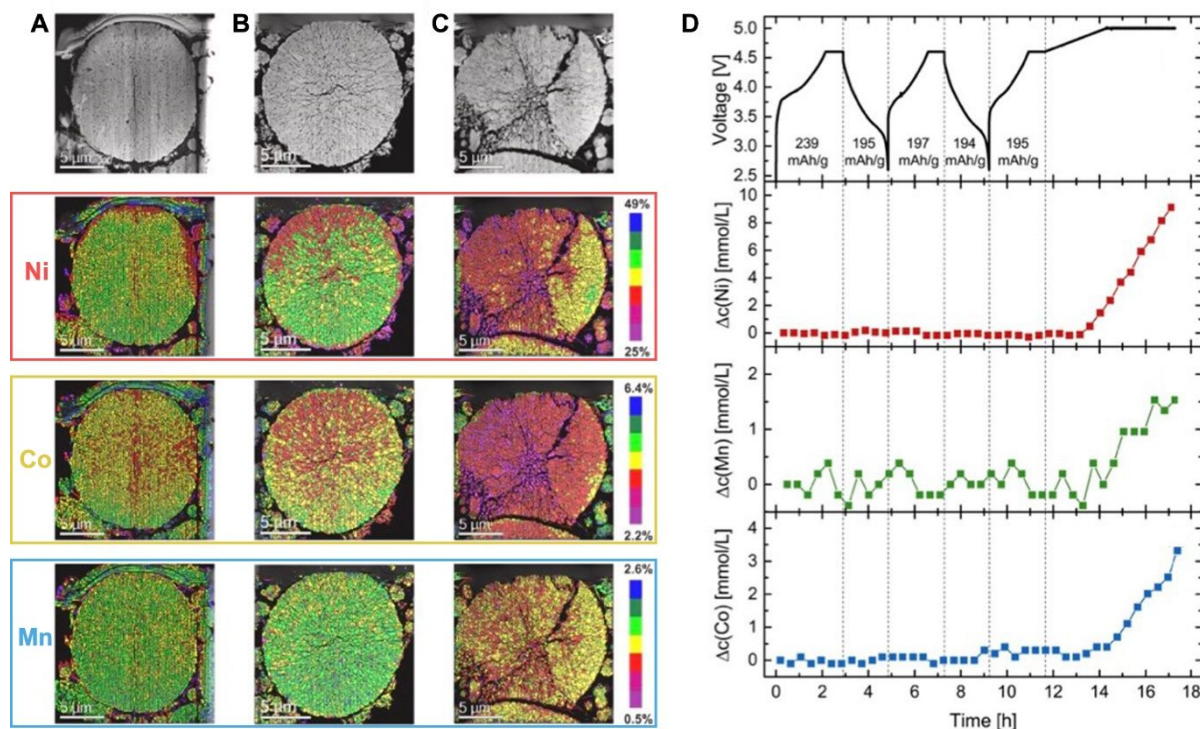


Fig. 9. Elemental mapping of Ni, Co, and Mn in $\text{LiNi}_{0.87}\text{Co}_{0.09}\text{Mn}_{0.04}\text{O}_2$ particles at (A) pristine, (B) cracked, and (C) broken states.¹¹³ (D) Effect of operating voltage on transition metal ion dissolution observed from a graphite side of an NCM622 Li-ion cell.¹¹⁴

4. Approaches to improve electrochemical properties of Ni-based layered oxide cathodes

Approaches to improving electro-chemo-mechanical stability of Ni-based layered oxide cathodes at fast charge has centered on various strategies to engineer charge carrier kinetics and suppress oxygen evolution.^{32, 115, 116} In this section, we will highlight effective approaches that can successfully modify physical, chemical, and morphological properties of NCM cathodes to achieve high reversible capacity.

4.1 Single crystalline particles

Ni-rich NCM undergoes anisotropic volume change at fast charge, leading to particle microcracking that creates newly exposed surface to the electrolyte, susceptible for gas evolution reactions.^{117, 118} Thus, controlling the orientation of NCM crystallites can be an effective means to preserve particle integrity.¹¹⁹ Single crystalline NCM cathodes have demonstrated improved mechanical and thermal stability.¹²⁰⁻¹²² Ma and coworkers engineered particle size of single crystal NCM622 to find a balance between rate capability and cycling stability.¹²³ They synthesized single crystal NCM622, in which average particle size is 2 μm by a molten-salt method, as observed by SEM in Fig. 10A. Electron backscatter diffraction (EBSD) of the cross-sectional particles in Fig. 10B indicates that as-synthesized NCM622 indeed consisted of single crystalline particles. EDS mapping in Fig. 10C and 10D shows uniform distribution of Ni, Co, and Mn in each particle. In Fig. 10E, the single crystal NCM622 cathode exhibited an excellent rate capability of 135 mAh g⁻¹ at 20 C, which is 75% of the capacity at 0.1C, while the polycrystalline NCM622 retained 80 mAh g⁻¹, 45% of its 0.1C capacity.

However, the morphology of single crystalline NCM particles is often non-spherical, making the cathode calendaring process difficult. Additionally, the single crystals tend to have larger particle size that leads to longer solid-state Li diffusion length, and thus sluggish Li kinetics, than the polycrystalline. Note that achieving a high Ni fraction in an NCM single crystal is non-trivial due to low synthesis temperature insufficient to promote grain growth.¹²² By hydrothermal synthesis, Lu et al.¹²⁴ obtained octahedron- (Fig. 10F) and polyhedron-shaped (Fig. 10G) single crystal NCM811 particles with controlled surface orientation and 1 μm average particle size. Fig. 10H demonstrates the rate capability of the two NCM811 particles and compares them with polycrystalline NCM811. While all NCM811 cathodes deliver a similar charge capacity of $\sim 200 \text{ mAh g}^{-1}$ at 0.1 C, the two single crystal NCM811 outperforms the polycrystalline at higher rates. Fig. 10I shows that polyhedron-shaped NCM811 does not develop surface phases after 100 cycles at 6C. The authors claimed that enhanced stability of single crystal NCM811 at fast charge is attributable to good rate capability. Density-functional theory (DFT) calculations further confirmed that (104) facets-dominated polyhedron-shaped particles have higher thermodynamic stability. The surface reconstruction is more likely to occur on the (012) facets compared with (104) facets, which is associated with the segregation of Ni to the surface and driven by the local distortions due to the mixing of Li ions and Ni ions.¹²⁵

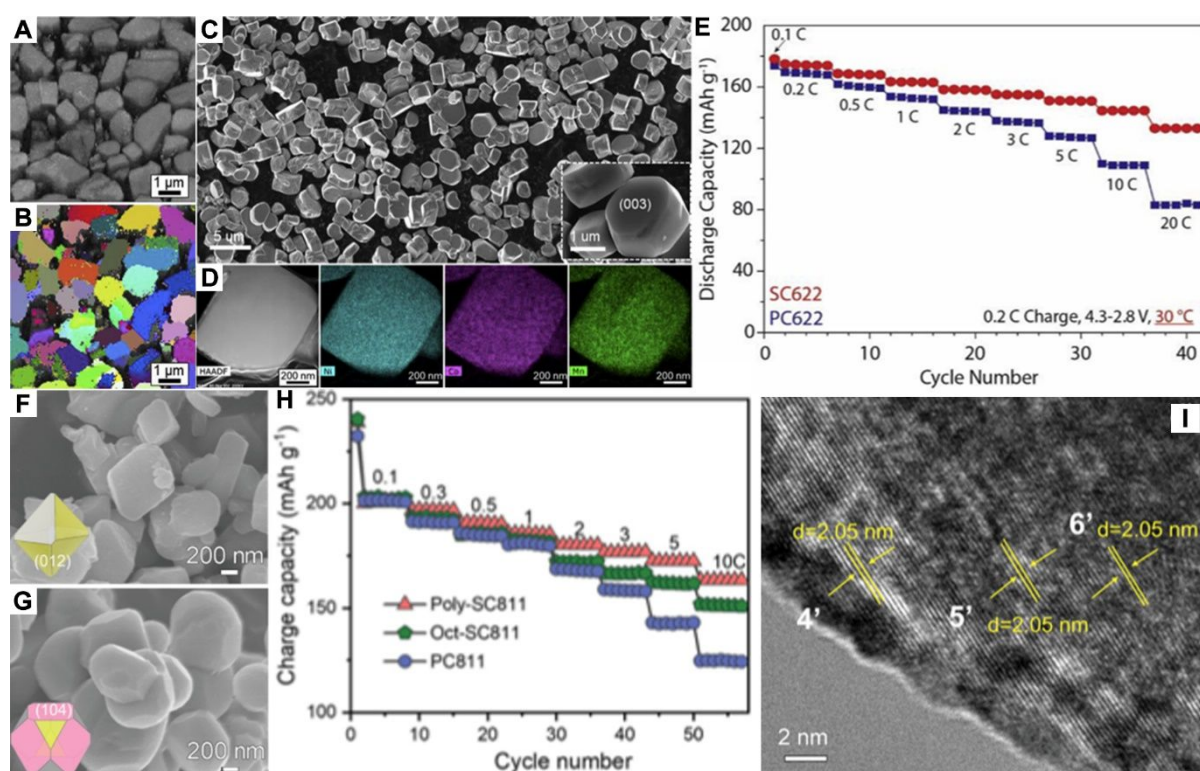


Fig. 10. (A) Band-contrast EBSD maps and (B) the EBSD orientation (Euler angles) map of the single crystal NCM622 particles.¹²³ (C) SEM image of the as-synthesized single crystal NCM622 particles.¹²³ (D) STEM-EDS mapping of the particle showing the homogeneous distribution of Ni, Co, and Mn elements.¹²³ (E) Rate capability of single crystal and polycrystalline NCM622 particles in terms of cycle number.¹²³ SEM images of (F) octahedron-shaped and (G) polyhedron-shaped single-crystalline NCM811 particles inserted with their schematic.¹²⁴ (H) The rate capability of polycrystalline NCM811, octahedron-shaped, and polyhedron-shaped NCM811.¹²⁴ (I) High resolution TEM microstructure of polyhedron-shaped NCM811 after 100 cycles at a 6 C rate.¹²⁴

4.2 Engineering particle morphology

The surface structure of Ni-based layered oxide particles is one of the factors that dictate Li kinetics.^{126, 127} Co-precipitation and subsequent solid-state reactions is the most common method to prepare Ni-based layered oxides,¹²⁸ and a wide variety of high-Ni NCM can be obtained by precisely controlling precursor stoichiometry and calcination parameters.^{129, 130} To achieve novel particle morphology that is unachievable by the conventional co-precipitation method for the Ni-based cathode, Su et al.¹³¹ employed two-step (secondary) co-precipitation that can lead to core-shell-structured NCM, as illustrated in Fig. 11A. The core structure was generated through the first co-precipitation process and then the active-plane-exposing shell was anchored on the core via the secondary co-precipitation. A cross-sectional SEM image and the associated schematic in Fig. 11B show this core-shell structure. The core particle was constructed by tetragonal-shape primary particles that can have high packing density while the surface shell exhibited a loose sheet-like structure with increasing surface area that can promote Li transport and charge transfer. This core-shell NCM811 delivered 160 mAh g⁻¹ at 10C.

Lai et al.¹³² employed ultrasound-triggered cation chelation to produce one-dimensional (1D) NCM622. For an aqueous solution of precursors, the ultrasonic wave can remove the hydration layer surrounding metal ions (step 1 in Fig. 11C) and promote a chelating reaction between the metal ions and ethylenediaminetetraacetic acid (EDTA) (step 2). The chelates can be separated from EDTA (step 3) and assembled into fiber-like structures by continuous ultrasonication (step 4), as shown in Fig. 11D. The obtained 1D NCM622 has the layered structure, as identified by HRTEM in Fig. 11E. This fibrous morphology provides continuous, percolated Li diffusion pathways at a nanometer scale, leading to high rate capability (122 mAh g⁻¹ at 10C).

Yuan et al.¹³³ reported improved cyclability for the LiNi_{0.8}Co_{0.15}Al_{0.05}O₂ (NCA) cathode by tailoring the surface characteristics of precursors using nondestructive plasma treatment with a mixed gas of O₂/Ar, as illustrated in Fig. 11F. The plasma treatment can expose pre-existing microvoids between primary precursor particles and form a layer of NiOOH with an ordered crystal structure on the surface, ensuring good layeredness of the entire particle. This plasma-treated precursor was mixed Li and calcined at 750°C for 12 h under O₂ atmosphere to obtain modified NCA. Fig. 11G shows rate capability of plasma-treated NCA (PTNCA), outperforming conventional NCA especially at high current density, which delivered ~170 mAh g⁻¹ at 5C. The improved rate capability can be plausibly explained by the effect of plasma treatment that creates the continuous layered structure throughout the particle, from bulk to surface, facilitating Li diffusion.

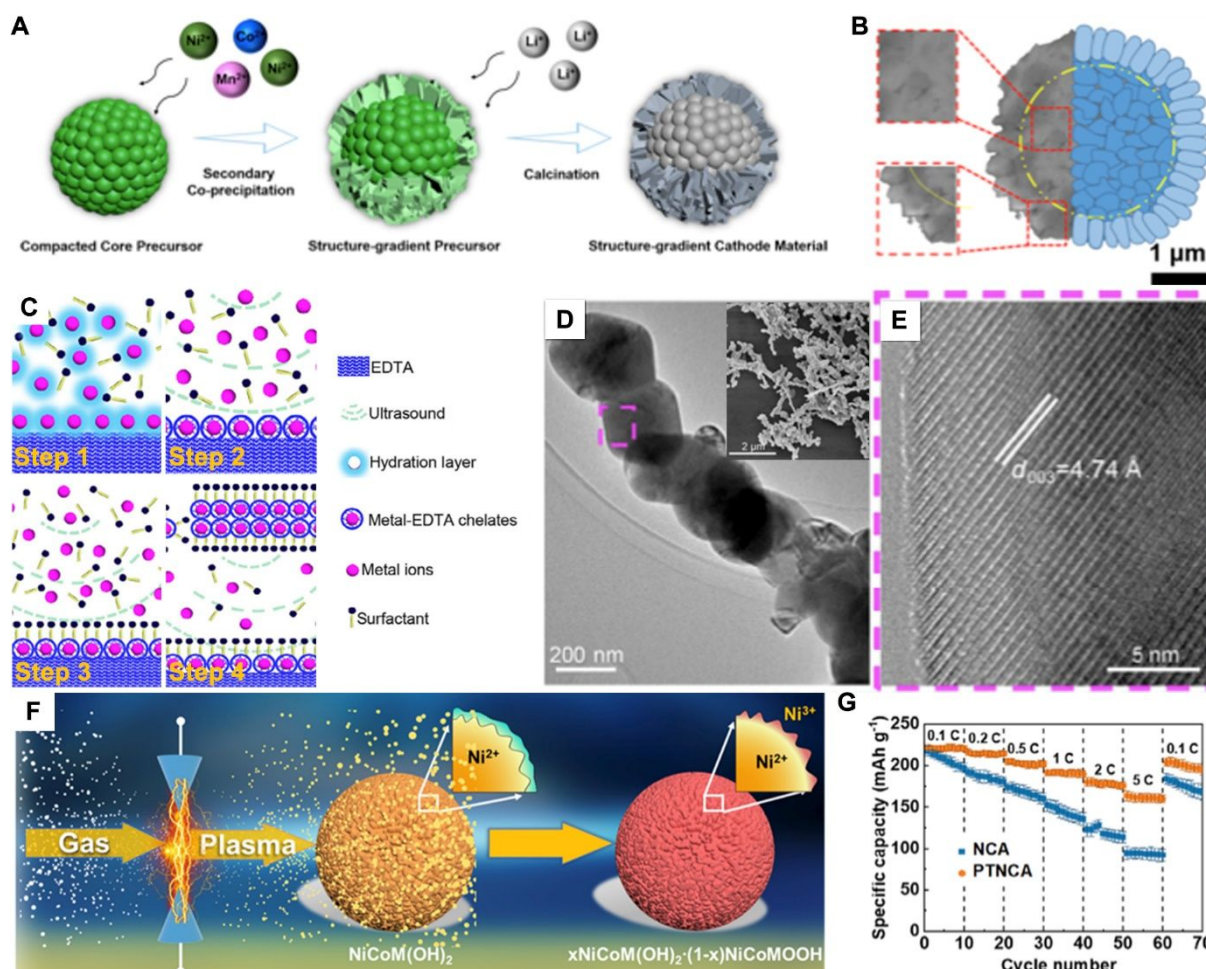


Fig. 11. (A) Schematic of the secondary coprecipitation method.¹³¹ (B) Cross-sectional SEM images of synthesized cathode materials along with schematic diagrams.¹³¹ (C) SEM images of one-dimensional NCM622 cathode materials. Inset, one-dimensional NCM622 cathode sample.¹³² (D) TEM image of one-dimensional NCM622 cathode material.¹³² (E) HRTEM image corresponding to the region taken from the pink dashed box in (D).¹³² (F) Schematic of plasma treatment.¹³³ (G) The rate capability of plasma treated NCA and bare NCA cathode.¹³³

4.3 Cation doping

Doping has been considered an effective way to enhance the electrochemical properties and chemical stability of the cathode.¹³⁴⁻¹³⁶ Table 2 summarizes the list of reported cation dopants. Intuitively, electrochemically inert elements, such as Mg^{2+} , Al^{3+} , and Zr^{4+} , as well as Mn^{4+} and Ti^{4+} , that does not participate in the redox reaction can stabilize delithiated structures and thus are favorable in general for battery materials design.¹³⁷⁻¹³⁹

Dopant	Function	Cathode material	Test parameter/ Cell structure	Electrolyte	Mass loading	Rate capability	Cycle retention	Ref
Mg	Improve the structure stability	NCM90	2.7-4.3 V / NCM90 Li	1 M LiPF ₆ in EC:EMC=3:7 (v/v) + 2 wt.% VC	12.0±0.5 mg cm ⁻²	~165 mAh g ⁻¹ (3 C)	80 (350 cycles under 0.33 C)	140
Nb	Improve the structure stability	NCM811	2.8-4.6 V / NCM811 Li	1 M LiPF ₆ in EC:DMC=1:1 (v/v)	15.0 mg cm ⁻²	~160 mAh g ⁻¹ (2 C)	92 (60 cycles under 0.33 C)	141
Fe	Improve the structure stability and decrease the particle size	LiNiO ₂	3.0-4.5 V / LiNiO ₂ Li	1 M LiPF ₆ in EC:DMC=1:1 (v/v)	/	~150 mAh g ⁻¹ (5 C)	96 (60 cycles under 1 C)	142
Cr	Improve the structure stability and decrease the particle size	LiNiO ₂	3.0-4.5 V / LiNiO ₂ Li	1 M LiClO ₄ in EC:DMC=1:1 (v/v)	/	~135 mAh g ⁻¹ (10 C)	95 (50 cycles under 1 C)	143
Sn	Improve the structure stability	NCM622	2.5-4.3 V / NCM622 Li	1 M LiPF ₆ in EC:DMC=1:1 (v/v)	/	~120 mAh g ⁻¹ (5 C)	90 (150 cycles under 1 C)	144
Ga	Improve the structure stability and Li ion transition kinetics	NCM811	2.8-4.3 V / NCM811 Li	1 M LiPF ₆ in EC:DMC:EMC=1:1:1 (v/v/v)	2.21 mg cm ⁻²	~120 mAh g ⁻¹ (10 C)	90 (100 cycles under 1 C)	145
Zr	Improve the structure stability and Li ion transition kinetics	NCM811	2.8-4.3 V / NCM811 Li	1 M LiPF ₆ in EC:EMC=3:7 (v/v)	4 mg cm ⁻²	~135 mAh g ⁻¹ (2 C)	85 (50 cycles under 0.2 C)	146
Ti	Improve the Li ion transition kinetics	NCM622	2.8-4.3 V / NCM622 Li	1 M LiPF ₆ in EC:DMC:EMC=1:1:1 (v/v/v)	/	~130 mAh g ⁻¹ (5 C)	/	147
Sb	Improve the structure stability	NC89	2.7-4.3 V / NC89 Li	1.2 M LiPF ₆ in EC:EMC=3:7 (v/v) + 2 wt.% VC	/	~195 mAh g ⁻¹ (2 C)	84 (1000 cycles under 1 C)	148
Mo	Improve the structure stability	NM90	2.7-4.3 V / NM90 Li	1.2 M LiPF ₆ in EC:EMC=3:7 (v/v) + 2 wt.% VC	4-5 mg cm ⁻²	~180 mAh g ⁻¹ (3 C)	86 (1000 cycles under 1 C)	149

Table 2. Summary of doping elements reported promoting the rate performance of LIBs.

Kim and Sun et al. investigated the effect of doping (Mn, Al, B, W, and Ta) on the microstructure of $\text{LiNi}_{0.91}\text{Co}_{0.09}\text{O}_2$.¹⁵⁰ In Fig. 12A, it can be seen that morphology of primary particles depends on doping elements: large equiaxed particles with Mn and Al and fine needle-like (preferred [003] orientation) particles with B, W and Ta. DFT was employed to theoretically confirm the surface energy modified by Ta and Al, through which the surface energies of (003) and (104) facets from both Ta-doped and Al-doped Ni-rich models were calculated. The results suggest that inducing ions with a larger ionic radius (i.e., Ta) lead to increase the surface energy on (104) facets rather than (003) facets, which indicates the higher stability of (003) facets in NCTa90 than in NCA90 cathode materials. Note that the equiaxed primary particles are also obtained in the pristine NCA. This needle-like morphology is expected to effectively dissipate strain energy of the Ni-rich layered oxide cathode upon charge and discharge as a significant amount of grain boundaries associated with ultrafine grains can deflect crack propagation compared with the large equiaxed particles.^{151, 152} These authors also explored mechano-chemical stability of Ni-rich cathodes upon Nb doping.¹⁵³ Nb was incorporated into NCA at the lithiation process of synthesis. As the doping content increases, the aspect ratio of NCA increases, transforming the equiaxed to elongated particles, as denoted in Fig. 12B. Specifically, Nb-doped Ni-rich primary particles are less than 400 nm wide with an average aspect ratio (particle length divided by width) of 6.3, whereas pristine Ni-rich primary particles are 200 nm – 1 μm wide with an average aspect ratio of 1.5. The orientation of the layered planes is parallel to the long axis of the elongated primary particles in Fig 12C, implying that Nb-doped NCA has a strong crystallographic texture. According to EDS line mapping across multiple particles, Nb was mostly found at the grain boundaries that likely function as Nb diffusion pathways.¹⁵³ Grain boundary pinning of Nb may stabilize the surface structure of NCA mechanically by suppressing lattice distortion and/or phase transformations of the layered phase. Indeed, Nb doping leads to a high-capacity retention of 93.1% ($\sim 170 \text{ mAh g}^{-1}$) for 500 cycles at a 3C rate.

It should be highlighted that cation doping has been sought to stabilize Co-free Ni-rich cathodes for high-power applications of Li-ion batteries. Park et al. used high-valence Mo^{6+} as a dopant to enhance electrochemical stability of $\text{LiNi}_{0.9}\text{Mn}_{0.1}\text{O}_2$ (NM90) upon delithiation and its Li kinetics.¹⁴⁹ As observed by TEM and the corresponding fast Fourier transform (FFT) in Fig. 12D, $\text{LiNi}_{0.89}\text{Mn}_{0.1}\text{Mo}_{0.01}\text{O}_2$ (Mo-NM90) charged at 4.4 V maintain the layered structure without signs of surface damage and intragranular fractures. To compare rate capability, $\text{LiNi}_{0.9}\text{Co}_{0.05}\text{Mn}_{0.05}\text{O}_2$ (NCM90), NM90, and Mo-NM90, were charged at two different rates alternatively between 0.5C and 3C. In Fig. 12E, Mo-NM90 demonstrates higher capacity retention rates ($\sim 200 \text{ mAh g}^{-1}$ at 0.5C and $\sim 174 \text{ mAh g}^{-1}$ at 3C) after 100 cycles at both rates than the others. Li diffusion can be 3 to 5 times faster along the grain boundaries than in bulk.¹⁴⁹ Given that Mo-NM90 exhibits fine primary particles, the improved charged state stability and high rate capability can be attributable to high grain boundary density as a result of Mo doping. However, introducing dopants may lead to the reduction of the discharge capacity such as Mg^{2+} , Al^{3+} and Ti^{4+} which are considered inactive in the layered structure of Ni-based oxide cathode materials. In addition, dopants like W^{6+} and Co^{3+} are expensive and, therefore, may result in higher costs of battery manufacturing.¹⁵⁴ Accordingly, cost-effective dopants that improve the overall electrochemical performance without reducing the discharge capacity need to be investigated and developed in the future.

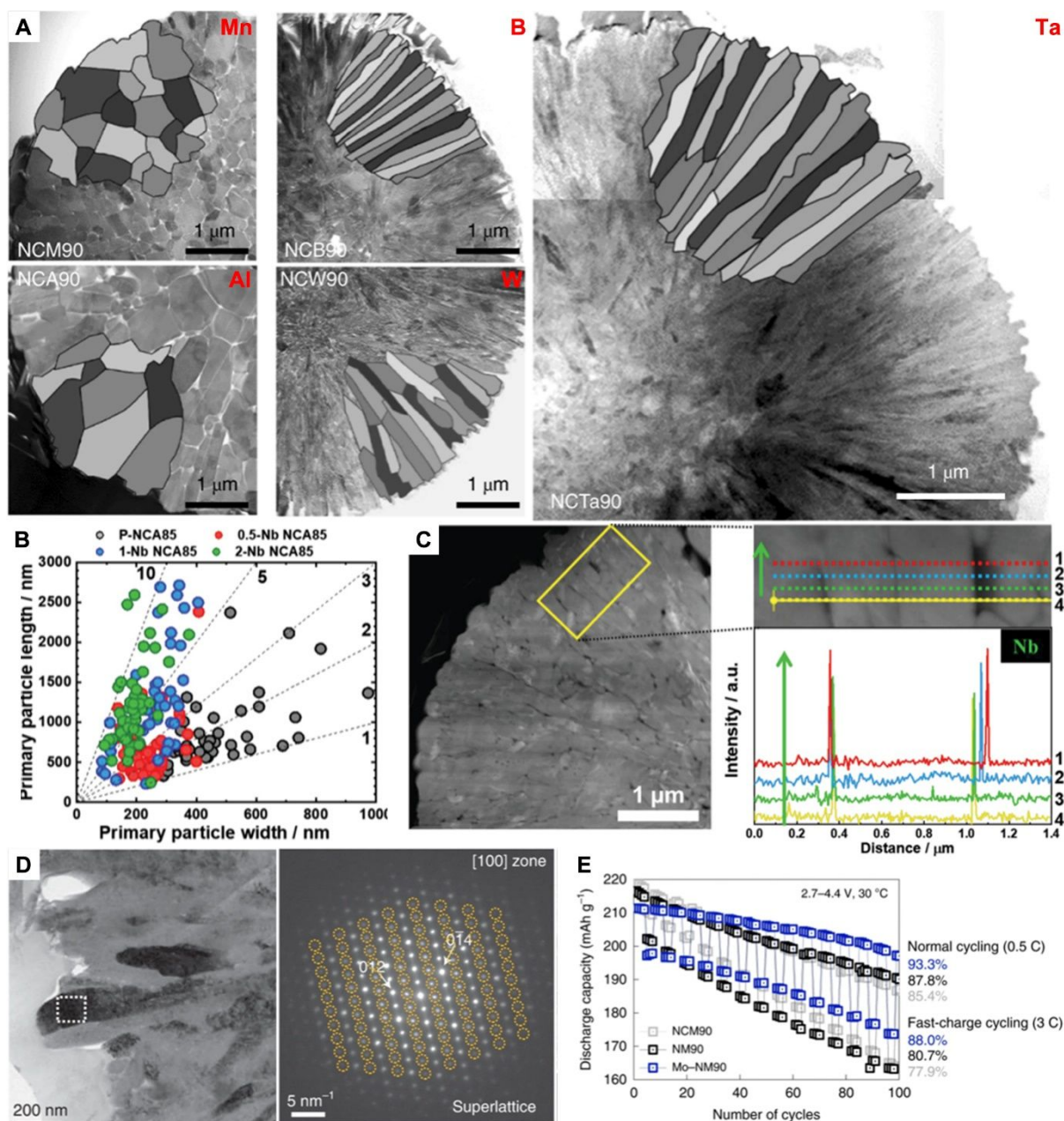


Fig. 12. (A) Scanning TEM image of a cross-sectional cathode particle and the corresponding schematic of the primary particles ($\text{Li}[\text{Ni}_{0.90}\text{Co}_{0.05}\text{Mn}_{0.05}]\text{O}_2$, $\text{Li}[\text{Ni}_{0.895}\text{Co}_{0.09}\text{B}_{0.015}]\text{O}_2$, $\text{Li}[\text{Ni}_{0.90}\text{Co}_{0.09}\text{Al}_{0.01}]\text{O}_2$, $\text{Li}[\text{Ni}_{0.90}\text{Co}_{0.09}\text{W}_{0.01}]\text{O}_2$ and $\text{Li}[\text{Ni}_{0.90}\text{Co}_{0.09}\text{Ta}_{0.01}]\text{O}_2$, denoted as NCM90, NCB90, NCA90, NCW90 and NCTa90, respectively).¹⁵⁰ (B) The aspect ratio of the primary particle.¹⁵³ (C) Plan-view TEM image of an Nb-doped NCA85 cathode and associated EDS line scans evaluating the Nb concentrations of the primary particles in the region marked with a yellow box.¹⁵³ (D) TEM image and SAED pattern of primary particle marked in D.¹⁴⁹ (E) Cycling performances of half cells featuring NCM90, NM90, and Mo-NM90 cathodes alternately charged at 0.5 C for four cycles and 3 C for three cycles at a time.¹⁴⁹

4.4 Coating

Coating has been widely used to tailor properties of cathode particles. Coating processes can also be compatible with other cathode optimization techniques such as cation doping and particle/grain size engineering by systematic experimental design. A wide variety of materials listed in Table 3 can be

used to coat primary particles (nanoscale), secondary particles (microscale), and the entire cathode (macroscale) using different methods.

Coating material	Cathode material	Test parameter/ Cell structure	Electrolyte	Mass loading	Rate capability	Cycle retention	Ref
LiF	NCM111	2.5-4.5 V / NCM111 Li	1 M LiPF ₆ in EC:DMC=1:1 (v/v)	/	~140 mAh g ⁻¹ (10 C)	89 (50 cycles under 1 C)	155
Li ₃ PO ₄	NCA	2.7-4.3 V / NCA Li	1 M LiPF ₆ in EC:DEC=1:1 (v/v)	4.5 mg cm ⁻²	~125 mAh g ⁻¹ (10 C)	88 (100 cycles under 0.5 C)	156
C ₆ H ₉ O ₆ La _x H ₂ O, C ₁₆ H ₃₆ O ₄ Ti (Dual)	NCM811	2.7-4.3 V / NCM811 Li	1 M LiPF ₆ in EC:DMC:EMC=1:1:1 (v/v/v)	2.3 mg cm ⁻²	~160 mAh g ⁻¹ (10 C)	90 (200 cycles under 1 C)	157
TiO ₂	NCM622	3.0-4.5 V / NCM622 Li	1 M LiPF ₆ in EC:DMC=1:1 (v/v)	/	~145 mAh g ⁻¹ (5 C)	89 (50 cycles under 1 C)	158
Li _x TiO ₂ -silica	NCM622	2.75-4.3 V / NCM622 Li	1 M LiPF ₆ in EC:DMC:EMC=1:1:1 (v/v/v)	4 mg cm ⁻²	~140 mAh g ⁻¹ (5 C)	91 (100 cycles under 0.5 C)	159
MgO	NCM523	3.0-4.3 V / NCM523 Li	1 M LiPF ₆ in EC:DEC=1:1 (v/v)	/	~120 mAh g ⁻¹ (10 C)	80 (180 cycles under 1 C)	160
MOF-derived alumina (MDA)	NCM622	3.0-4.5 V / NCM622 Li	1 M LiPF ₆ in EC:DMC=1:1 (v/v)	2-3 mg cm ⁻²	~150 mAh g ⁻¹ (10 C)	92 (100 cycles under 1 C)	161
PEDOT	NCM811	3.0-4.3 V / NCM811 Li	1 M LiPF ₆ in EC:DMC:EMC=1:1:1 (v/v/v)	3.6 mg cm ⁻²	~170 mAh g ⁻¹ (7 C)	80 (300 cycles under 1 C)	162
Co _x B	NCM811	3.0-4.4 V / NCM811 Li	1 M LiPF ₆ in EC:DMC:EMC=3:3:4 (v/v/v) + 5 wt. % FEC	10.5±0.2 mg cm ⁻²	~200 mAh g ⁻¹ (7 C)	82 (200 cycles under 7 C)	163

Table 3. Summary of coating materials reported promoting the rate performance of LIBs.

Li et al. employed atomic layer deposition (ALD) to directly apply a thin layer of LiTaO_3 coating on the surface of the NCM111 cathode.¹⁶⁴ Fig. 13A compares the surface texture of the NCM particles before and after the ALD coating process and shows a uniform and conformal ALD layer. The EDS result in Fig. 13B clearly indicates that Ta-rich coating (~ 5 nm) is formed on the particle. Fig. 13C shows rate capability tests of ALD-coated NCM cathodes. Optimized ALD-coated NCM111 delivers high capacity, cyclability, and high rate capability. At 700 mA g^{-1} , NCM111 coated with five ALD layers (NMC-5 in Fig. 13C) achieves high discharge capacity of 125 mA h g^{-1} , 77% of the capacity obtained at 100 mA g^{-1} . While thin coating unlikely impedes Li diffusion across the cathode-electrolyte interface, thick ALD coating leads to poor rate capability for the NCM cathode (e.g., NMC-10 in Fig. 13C)

Oxidative chemical vapor deposition (oCVD) that leverages deep penetration of carrier gases into porous media is another effective method to conformally coat NCM particles. As illustrated in Fig. 13D, Xu et al. used oCVD to apply poly(3,4-ethylenedioxythiophene) (PEDOT) coating on primary and secondary NCM particles simultaneously.¹⁶⁵ At high-voltage charging in $4.3 - 4.6 \text{ V}$, in situ XRD in Fig. 13E shows continuous peak shifting but no peak splitting, indicating the integrity of the layered phase as a result of PEDOT coating, likely dissipating strain energy associated with volume change of the H3 phase. Zhang et al. demonstrated that PEDOT coating by oCVD can be directly applicable to cathodes in a larger scale (Fig. 13F).¹⁶² NCM811 cathodes with PEDOT coating outperforms pristine NCM 811 for high rate capability and cyclability. In Fig. 13G, discharge capacities of PEDOT-coated and pristine NCM811 obtained at 7C are 170 and 150 mAh g^{-1} , respectively. In subsequent 0.1C discharge, coated NCM recovers the full initial capacity, while pristine NCM shows substantial capacity loss, indicative of structural and chemical damages in the particles.

Similarly, Choi and coworkers developed a coating-plus-infusion method to passivate both primary and secondary particles.¹⁶³ They demonstrated that as-synthesized Co_xB can completely coat the secondary particles and subsequently infiltrate into interfaces between the primary particles (Fig. 13H). The cycling stability of NCM811 was dramatically improved by this infused microstructure at high discharge rates (up to $1,540 \text{ mA g}^{-1}$). It should be pointed out that these tests were performed at $45 \text{ }^\circ\text{C}$, which generally shows fast Li kinetics unless the structure is unstable. The rate performance of Co_xB -coated NCM811 and pristine NCM811 at $25 \text{ }^\circ\text{C}$ is shown in Fig. 13I. The Co_xB -coated NCM811 cathode delivers a specific capacity $\sim 175 \text{ mAh g}^{-1}$ at 10 C compared with $\sim 140 \text{ mAh g}^{-1}$ of pristine NCM811, indicating that Co_xB coating-and-infusion can enhance the rate capability and cycling stability of NCM. To reveal the functionality of the amorphous Co_xB coating layer on the electrochemical performance of the NCM811 cathode material, DFT calculations were conducted to unveil that the strength of Co-O and B-O bonds is stronger than Ni-O bonds. The results indicate the strong covalent B-O and Co-O bonds stabilized the interface O, which enhanced the electronic-structure stability, and hence the rate capability and cycling stability. The coating layers achieved by novel methods such as ALD and oCVD are conformal and thickness controllable. However the overall cost leveraging the ALD and oCVD techniques may increase and the precursor materials of these methods are limited, depending on the reaction mechanisms. More economical strategies such as hydrothermal, solid state, and sol-gel processes are available on large scale electrodes with easier selection of coating materials. However, the coating layer by these conventional approaches is less uniform and conformal (or low step coverage) for Ni-based layered oxide particles, compared to those by novel techniques.¹⁵⁴ The uncoated regions

due to the non-uniformity of the conventional will be directly exposed to the electrolyte and result in performance fading due to electrolyte oxidation. Therefore, the affordable coating methods realizing high coverage and uniformity is required.

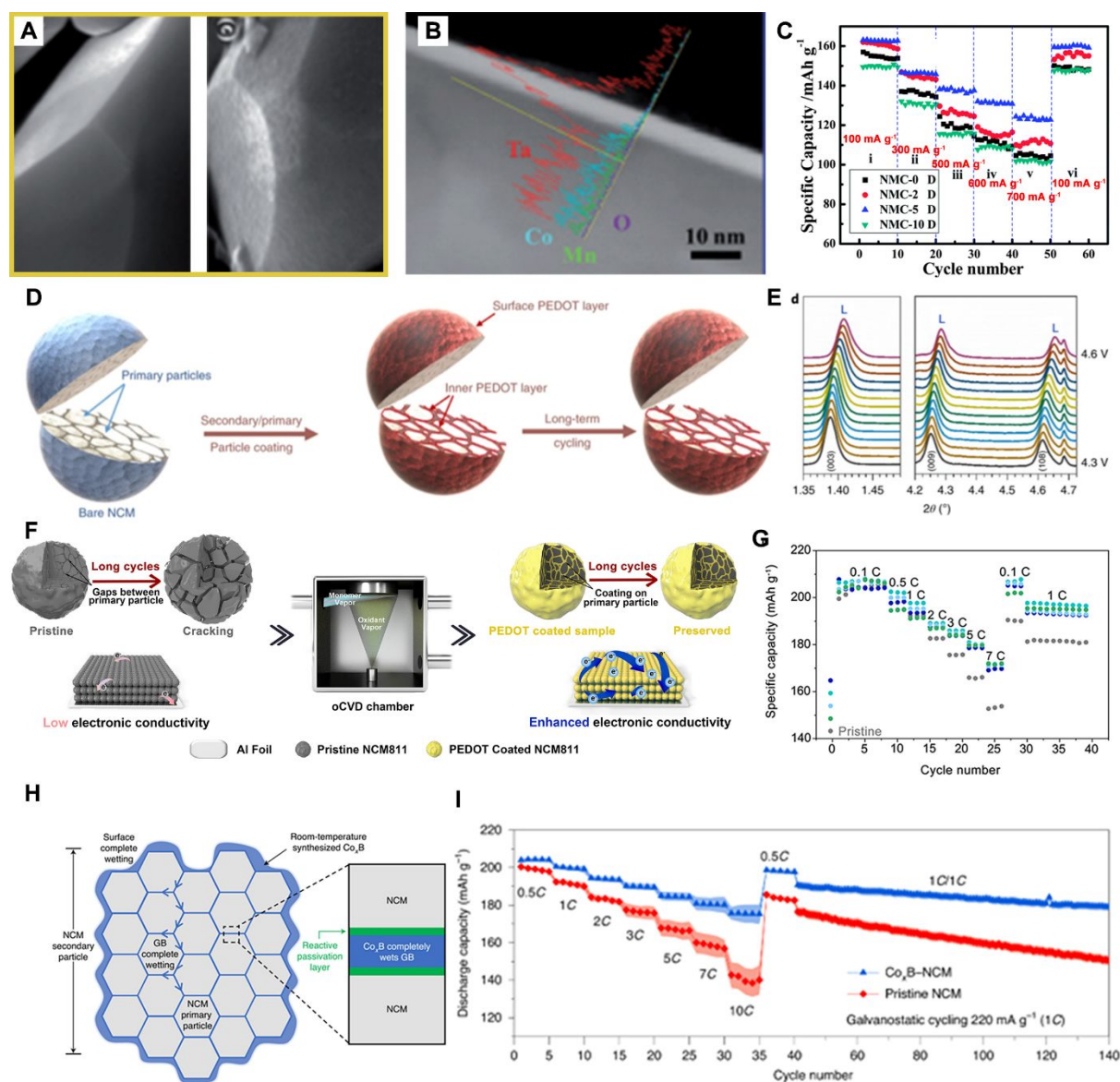


Fig. 13. (A) Typical morphologies of Pristine and ALD LiTaO_3 modified NCM111 and (B) linear EDX scan of ALD modified NCM.¹⁶⁴ (C) The rate capability of various ALD-modified NCM cathodes.¹⁶⁴ (D) An illustration of the structural stability of both primary particle and secondary particle coating via oCVD after long-term cycling.¹⁶⁵ (E) Selected in situ high-energy XRD patterns from oCVD PEDOT-coated cathodes in the high-voltage (4.3–4.6 V) region during the charge process.¹⁶⁵ (F) Schematic of vapor-phase synthetic process of Ni-rich cathode modified with highly conformal oCVD PEDOT.¹⁶² (G) The rate capability of various kinds of PEDOT coated NCM cathode.¹⁶² (H) Schematic coating-plus-infusion microstructure in which Co_xB uniformly coats the surface of NCM secondary particles and infuses grain boundaries between the NCM primary particles.¹⁶³ (I) 7 C cycling tests in the range of 3.0–4.4 V versus Li/Li^+ at 45°C .¹⁶³

4.5 Electrolyte additives

The localized inhomogeneity at the particle- and electrode-levels induced by fast-charging can lead to partial over-delithiation in Ni-rich NCM (Section 3.1). Highly oxidized Ni ion (Ni^{4+}) is unstable by nature and can be readily reduced to Ni^{3+} and Ni^{2+} by oxidizing surrounding oxygen (i.e., oxygen gas evolution). If Ni^{4+} oxidizes electrolyte molecules, electrolyte decomposition products known as cathode-electrolyte interphases (CEIs) that increase cell impedance can form. Functional additives to the electrolyte can address problems associated with undesirable Ni reduction by increasing anodic stability of the electrolyte as well as changing the composition of CEIs. Indeed, designing uniform cathode-electrolyte interphases (CEI) that have self-limiting thickness to provide robust particle passivation while permitting facile Li diffusion key to developing next-generation cathodes for high-voltage, fast charging Li-ion batteries. Table 4 summarizes electrolyte additives used to improve electrochemical properties of Ni-rich layered oxide cathodes.

Additive	Cathode material	Test parameter/ Cell structure	Electrolyte	Mass loading	Rate capability	Cycle retention	Ref
[4,4'- bi(1,3,2-dioxathiolane)]2,2'-dioxide	NCM532	3.0-4.6 V / NCM532 Li	1 M LiPF ₆ in EC:EMC=3:7 (v/v)	22.5 mg cm ⁻²	~160 mAh g ⁻¹ (10 C)	92 (100 cycles under 0.5 C)	166
p-toluenesulfonyl isocyanate	NCM532	3.0-4.6 V / NCM532 Li	1 M LiPF ₆ in EC:EMC=3:7 (v/v)	1.8 mg cm ⁻²	~120 mAh g ⁻¹ (10 C)	86 (100 cycles under 1 C)	167
qisophorone diisocyanate	NCM532	2.5-4.6 V / NCM532 Li	1 M LiPF ₆ in PC:DMC=1:1 (v/v)	/	~150 mAh g ⁻¹ (5 C)	83 (200 cycles under 1 C)	168
lithium difluorophosphate	NCM532	2.8-4.6 V / NCM532 Graphite	1 M LiPF ₆ in EC:DEC=1:3 (wt/wt)	31.38 mg cm ⁻²	~120 mAh g ⁻¹ (5 C)	62 (160 cycles under 0.5 C)	169
tris(trimethylsilyl)phosphite	NCM622	2.8-4.45 V NCM622 MCMB	1 M LiPF ₆ in EC:DMC:EMC=1:1:1 (v/v/v)	11.7 mg cm ⁻²	~130 mAh g ⁻¹ (5 C)	79 (300 cycles under 1 C)	170
diphenyldimethoxysilane	NCM622	2.8-4.3 V / NCM622 Li	1 M LiPF ₆ in EC:DMC:EMC=1:1:1 (v/v/v)	1.52 mg cm ⁻²	~143 mAh g ⁻¹ (10 C)	99 (200 cycles under 2 C)	171
3-isocyanatopropyltriethoxysilane	NCM622	2.5-4.5 V / NCM622 Li	1 M LiPF ₆ in EC:DMC:EMC=1:1:1 (v/v/v)	2.76-3.46 mg cm ⁻²	~120 mAh g ⁻¹ (10 C)	73 (159 cycles under 0.3 C)	172
succinic anhydride	NCM811	2.8-4.3 V / NCM811 Graphite	1 M LiPF ₆ in EC:EMC=3:7 (v/v)	10 mg cm ⁻²	~150 mAh g ⁻¹ (5 C)	94 (400 cycles under 1 C)	173
N-allyl-N,N-bis(trimethylsilyl)amine	NCA85	3.0-4.2 V / NCA85 Li	1 M LiPF ₆ in EC:DEC:EMC=3:2:5 (v/v/v)	3.68 mg cm ⁻²	~100 mAh g ⁻¹ (7 C)	86 (300 cycles under 1 C)	174
1,2,4-1 <i>H</i> -Triazole	NCM90	3.0-4.3 V / NCM90 Li	1 M LiPF ₆ in EC:DEC=3:7 (v/v)	3-4 mg cm ⁻²	~175 mAh g ⁻¹ (10 C)	87 (150 cycles under 1C)	175
LiDFOB	LiNiO ₂	2.7-4.4 V / LiNiO ₂ Li	1 M LiPF ₆ in FEC:FEMC:HFE=2:6:2 (wt/wt/wt)	3 mg cm ⁻²	~120 mAh g ⁻¹ (5 C)	80 (400 cycles under 0.5 C)	176

Table 4. Summary of electrolyte additives reported promoting the rate performance of LIBs.

Sun and coworkers reported that succinic anhydride (SA) addition to the carbonate electrolyte enhances the rate capability of Li/NCM811 cells.¹⁷³ A DFT calculation was conducted to compare the highest occupied molecular orbital (HOMO) energies of SA molecules and molecules of the electrolyte solvent. Through Gauss fitting, the value of HOMO energies of SA, EC, and EMC were determined to be about -6.45 eV, -8.50 eV, and -8.20 eV, respectively, indicating the SA molecules are oxidized preferentially at the cathode during the charging process. They found that SA induces uniform CEI that prevents internal cracking from the inside of secondary particles (Fig. 14A). Electrochemical impedance spectroscopy (EIS) in Fig. 14B shows that impedance, as a lump sum of interphase and charge transfer resistance contributions, for the cell with SA after 100 cycles is much smaller than the cell without it. This result suggests that SA-related CEI can passivate and stabilize the high-voltage structure of NCM811 particles at fast charge ($\sim 150 \text{ mAh g}^{-1}$ at 5C). For a Ni-rich ($\text{Ni} \geq 0.9$) layered oxide cathode, $\text{LiNi}_{0.9}\text{Co}_{0.05}\text{Mn}_{0.05}\text{O}_2$ (NCM90), Zou et al. used 1,2,4-1H-Triazole (HTZ) as the electrolyte additive that can reduce solution resistance and tailor CEI compositions.¹⁷⁵ Similarly, the HOMO/lowest unoccupied molecular orbital (LUMO) values of EC, DEC, and HTZ were compared through DFT calculations. The higher HOMO value and lower LUMO value of HTZ suggest the HTZ would be preferably oxidized at the cathode and reduced at the anode than with the EC and DEC molecules in electrolyte, generating CEI and SEI layer on the cathode and anode respectively. Fig. 14C plots specific capacity of the NCM90 cathodes with the baseline electrolyte and 0.3% HTZ-containing electrolyte as a function of discharge rates for multiple cycles. By introducing HTZ to the electrolyte, the NCM90 cathode demonstrates improved rate capability ($\sim 175 \text{ mAh g}^{-1}$ at 10C) and capacity retention (87% after 150 cycles). This result corroborates with SEM and TEM images in Figs. 14D and E, which show clean NCM90 particles with uniform CEI after cycling with the HTZ-added electrolyte.

In addition to oxidation stability against the cathode, judicious selection of additives can enhance electrolyte's reduction stability against the anode. Lu and coworkers reported the effect of lithium tetrafluoroborate (LiBF_4) and lithium nitrate (LiNO_3) on electrochemical stability of a carbonated-based electrolyte.¹⁷⁷ These dual-salt additives can form stable CEIs on the primary particles of NCM811, as observed by HRTEM in Fig. 14F, and possibly form stable solid-electrolyte interphases (SEIs) on the anode surface (Fig. 14G), promoting Li kinetics across the entire cell and cycling stability. In Fig. 14H, conventional ethylene carbonate (EC)/diethyl carbonate (DEC) does not sustain the high voltage cutoff (4.4 V) of a Li/NCM811 half-cell at rates higher than 0.3C. In contrast, the cell with fluoroethylene carbonate (FEC)/ethyl methyl carbonate (EMC) shows respectable rate capability even without additives. Fluorides are favorable interphase compositions due to high reduction and oxidation stability,^{178, 179} and thus fluorination of CEIs and SEIs by decomposing FEC likely enables reversible Li intercalation at high rates. While LiBF_4 addition to the FEC/EMC electrolyte alone does not improve Li intercalation kinetics much, the dual-salt additives lead to substantial increase in high rate capacity, showing 185.6 mAh g^{-1} at 5C ($\sim 10 \text{ mA cm}^{-2}$). It is likely that electrically conductive nitrides may form in the interphases, reducing the charge transfer kinetics at high rates. Noteworthy, the electrolyte additive (e.g., salt-type) may be reduced and decomposed at the anode side in full cells due to the low LUMO level of these additives and will not form a suitable CEI on the cathode. Besides, some types of electrolyte additives are detrimental to the anode material (e.g., Si-based), which should be utilized with other compounds to build F-donating SEI protection layer for the Si anode.¹⁸⁰

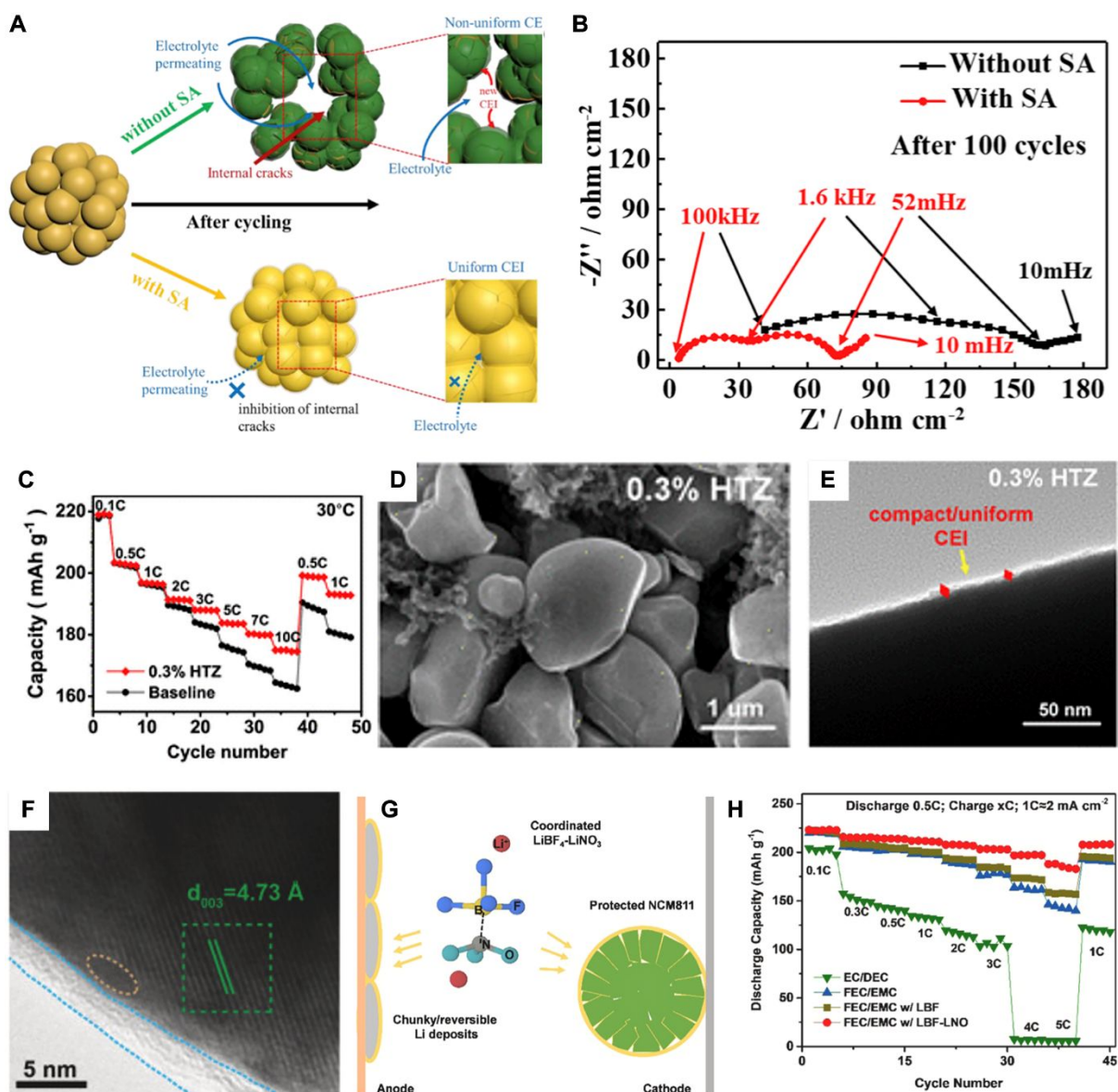


Fig. 14. (A) Schematic illustration of the protection mechanism of CEI formed by SA.¹⁷³ (B) Nyquist plots of Li/NCM811 cells after 100 cycles.¹⁷³ (C) Rate performance of the HTZ-additive and baseline cells at 30 °C.¹⁷⁵ (D) SEM and (E) TEM images of NCM90 electrodes after 150 cycles.¹⁷⁵ (F) HRTEM images of NCM811 cycled in electrolyte with dual additives after 100 cycles.¹⁷⁷ (G) Schematic of dual-salt-additives working on both cathode and anode.¹⁷⁷ (H) Charging at an increasing C rate but discharging at a constant 0.5 C rate.¹⁷⁷

4.6 Electrode architectures.

While conventional cathode construction that mixes active NCM particles uniformly with activated carbon and a binder is non-directional at a macroscopic scale, electric field developed in the cathode upon charge and discharge is directional at a microscopic scale. Thus, the SoC for individual NCM particles (i.e., different Li concentration) may be different from each other, especially if charge carrier and electron conduction pathways are poorly percolated, developing local inhomogeneity in the cathode upon charge and discharge. This kinetic limitation known as polarization increases as a charging rate increases (i.e., fast-charging). Therefore, fast charge performance of NCM cathodes can be improved

by tailoring electrode architectures.

To develop thick electrodes for high energy density, Wood et al. investigated how particle size distribution of a Ni-based layered oxide cathode and the graphite anode affects specific capacity as a function of rates.¹⁸¹ Fig. 15A shows five different electrode configurations: 1) single-sized small (6 μm) particles, 2) random mixing of small and large (12 μm) particles, 3) layer-by-layer where large particles are near the current collector, 4) layer-by-layer where small particles are near the current collector, and 5) single-sized large particles. In Fig. 15B, although rate capability is poor for all cases due to thick electrode construction, cathode configuration 3) provides the highest 2C capacity of 100 mAh g^{-1} in combination with anode configuration 4), among others. This result can suggest that tortuosity of the porous electrode and the particle size distribution play a critical role in Li kinetics, while clear understanding is lacking. Hu et al. argued that cathode calendaring can physically enhance Li transport and electron conduction in the cathode.¹⁸² As shown in Fig. 15C, Li ion can migrate inside the cathode through the porosity where large free volume for electrolyte penetration exists. In this case the cathode is charge transfer-limited as electronic conduction is not percolated. Calendaring provides high packing density, leading to effective percolation of both Li and electron pathways. Note that over-calendaring may lead to particle cracking and/or reduce electrolyte penetration that decreases the number of accessible Li at fast charge. These exercises suggest a balance between high energy density (packing fraction) and high power (tortuosity) can be achieved by engineering electrode configurations.

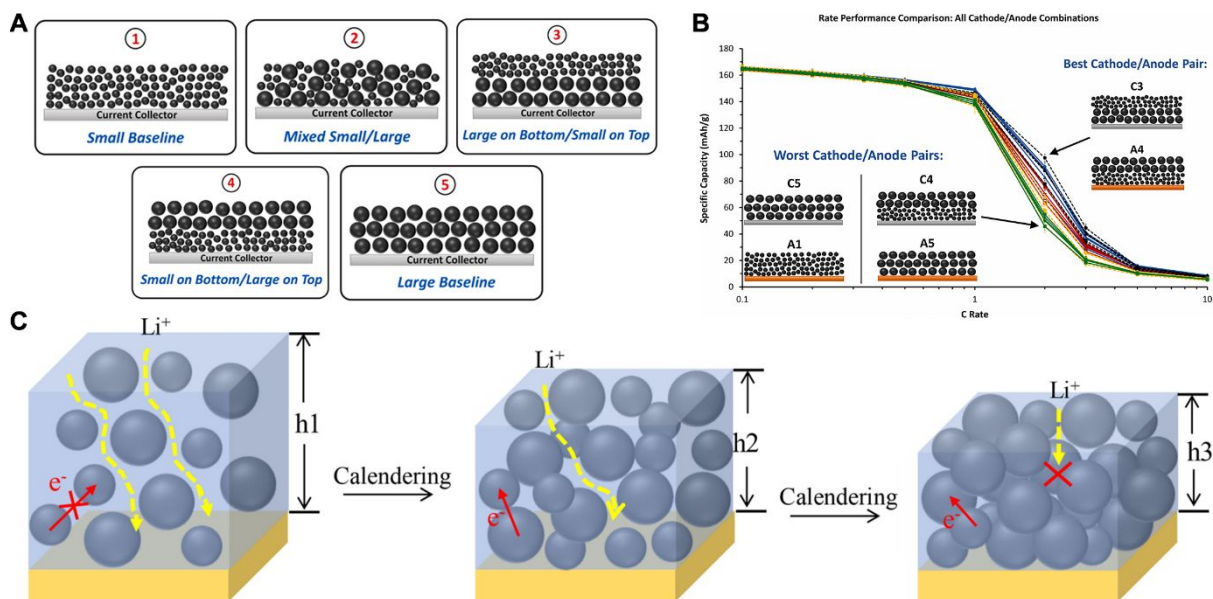


Fig. 15. (A) Thick electrode designs with different active material particle sizes and configurations.¹⁸¹ (B) Rate performance comparison for single-layer pouch cells made with all 25 cathode/anode design combinations.¹⁸¹ (C) Sketch of cathode calendaring from high thickness (h_1) to low thicknesses (h_2 and h_3 , $h_2 > h_3$).¹⁸²

5. Summary and Outlook

Rapidly increasing EV production demands next-generation Li-ion batteries. Ni-based layered oxides are the strongest cathode system for the future EV technology due to the potential for high capacity at a reasonable cost. Many car makers have implemented the Ni-rich cathode in battery packs for their

EVs. However, pushing to the limit of the Ni content in the layered oxide cathodes faces challenges due to electrochemical degradation especially at fast-charging and high voltage.

This review discusses the degradation mechanisms of Ni-based cathodes at fast charge in various length scales. Chemical and mechanical inhomogeneities developed in charged Ni-rich layered oxides is critical to determining the rate capability and cyclability of the cathode. The electrode level inhomogeneity is attributed to the non-uniform SoC in individual particles, leading to microcracks in particles and local delamination of the electrode. The single particle-level inhomogeneity results in the different degrees of delithiation. Local overcharge leads to oxygen loss from layered oxides, inducing electrolyte oxidation, irreversible phase transformations (from layered to spinel and to rock-salt phase), and transition metal dissolution, all of which lead to sudden cell failure. Of note, the fast charging process will accelerate the oxygen loss due to large polarization.

Strategies to improve rate capability and cyclability of Ni-rich layered oxide cathodes include, but not limited to, synthesis optimization (modified co-precipitation), single crystal growth, engineering of electrolyte additives, cation doping, protective surface coating, and cathode architecture design. To summarize recent progresses in the development of Ni-based layered oxide cathode can be envisioned as below:

- (1) Tailoring the size, shape, and combination of primary particles of Ni-based layered oxides to reduce local overcharging;
- (2) Functional coating, doping or designing zero-strain composition to enhance electrochemical and chemical stability of Ni-based layered oxides by suppressing oxygen loss;
- (3) Electrode construction with engineered thickness and tortuosity to promote rate capability and energy density;

It should be emphasized that addressing complex problems present in modern cathodes by one approach is highly unlikely as electrochemical and physicochemical properties are strongly coupled. A holistic approach leveraging multiple strategies is therefore required to enable fast charging Ni-rich layered oxides for emerging EV applications.

Acknowledgement

S.L. and H.W.S. acknowledge the support from the Improvement of Measurement Standards and Technology for Mechanical Metrology (Grant No. 22011044) by KRISS. S.L. also thanks a partial support from NSF, Award number CBET-2207302. J.C.K. is grateful for support from the PSEG Foundations to advance energy innovation at Stevens.

Bio:

Yuxuan Zhang received his bachelor's and Master's degree in Materials Science and Engineering from the University of Science and Technology Beijing in 2016 and 2019 respectively. He is currently a Ph.D. student in School of Engineering Technology at Purdue University, under the supervision of Professor Sunghwan Lee. His research primarily focuses on the design and optimization of the electrode materials for high energy density Li-ion batteries.

Dr. Jae Chul Kim is an assistant professor of Chemical Engineering and Materials Science at Stevens Institute of Technology. He received his Ph.D. degree in Materials Science and Engineering in 2014 from Massachusetts Institute of Technology (MIT) and finished his postdoctoral training at MIT and Lawrence Berkeley National Laboratory before joining Stevens in 2018. His research focus centers on understanding and exploiting the underlying chemical and electrochemical reactions and processes of energy storage systems. He is a recipient of the 2022 DOE Early Career Research Program Award.

Dr. Han Wook Song is a Principal Research Scientist at Korea Research Institute of Standards and Science (KRISS). He earned his Ph.D. degree in Materials Science and Engineering from KAIST. His research focuses on vacuum processing, tactile sensors, and energy devices.

Dr. Sunghwan Lee is an assistant professor of Engineering Technology at Purdue University. He received the Ph.D. degree in Materials Science from Brown University in 2013. He was a post-doctoral scientist at MIT and Harvard University from 2013 to 2015. His research interests are focused on the discovery of functional thin film materials and their integration in various applications including energy storage devices, transparent and flexible electronics, and sensors.

References:

1. A. L. Stephen Nalley, International Energy Outlook 2021, <https://www.eia.gov/outlooks/ieo/>, (accessed October 6th, 2021).
2. T. U. S. E. P. Agency, Inventory of U.S. Greenhouse Gas Emissions and Sinks: 1990-2019, <https://www.epa.gov/ghgemissions/inventory-us-greenhouse-gas-emissions-and-sinks-1990-2019>, (accessed April, 2021).
3. G. Motors, GM Corporate Newsroom, <https://media.gm.com/media/us/en/gm/home.detail.ht>).
4. F. M. Company, Ford Media Center, <https://media.ford.com/content/fordmedia/fna/us/en>).
5. T. Nagaura and K. Tozawa, *JEC Press*, 1990, **9**, 209.
6. M. Armand and J. M. Tarascon, *Nature*, 2008, **451**, 652-657.
7. L. Lu, X. Han, J. Li, J. Hua and M. Ouyang, *Journal of Power Sources*, 2013, **226**, 272-288.
8. J. B. Goodenough and K.-S. Park, *Journal of the American Chemical Society*, 2013, **135**, 1167-1176.
9. BloombergNEF, Electric Vehicle Outlook 2021, <https://bnef.turtl.co/story/evo-2021/page/1?teaser>).
10. M. S. Whittingham, *Chemical Reviews*, 2004, **104**, 4271-4302.
11. J. Zhang, H. Zhong, C. Zheng, Y. Xia, C. Liang, H. Huang, Y. Gan, X. Tao and W. Zhang, *Journal of Power Sources*, 2018, **391**, 73-79.
12. Y. Zhu, S. He, J. Ding, G. Zhao and F. Lian, *Nano Research*, 2022, DOI: 10.1007/s12274-022-4852-y.
13. W. Li, E. M. Erickson and A. Manthiram, *Nature Energy*, 2020, **5**, 26-34.
14. W. Liu, P. Oh, X. Liu, M.-J. Lee, W. Cho, S. Chae, Y. Kim and J. Cho, *Angewandte Chemie International Edition*, 2015, **54**, 4440-4457.
15. Y.-K. Sun, S.-T. Myung, B.-C. Park, J. Prakash, I. Belharouak and K. Amine, *Nature Materials*, 2009, **8**, 320-324.
16. P. Morrissey, P. Weldon and M. O'Mahony, *Energy Policy*, 2016, **89**, 257-270.
17. A. Meintz, J. Zhang, R. Vijayagopal, C. Kreutzer, S. Ahmed, I. Bloom, A. Burnham, R. B. Carlson, F. Dias, E. J. Dufek, J. Francfort, K. Hardy, A. N. Jansen, M. Keyser, A. Markel, C. Michelbacher, M. Mohanpurkar, A. Pesaran, D. Scofield, M. Shirk, T. Stephens and T. Tanim, *Journal of Power Sources*, 2017, **367**, 216-227.
18. f. r. c. NACS, The US Petroleum Industry Statistics, <http://www.nacsonline.com/YourBusiness/FuelsCenter/Basics/Articles/Pages/The-US-Petroleum-Industry-Statistics-Definitions.aspx#.WESTQHRN7hE>, (accessed December 4, 2016).
19. M. Li, M. Feng, D. Luo and Z. Chen, *Cell Reports Physical Science*, 2020, **1**, 100212.
20. T. D. David Howell, Peter Faguy, Brian Cunningham, US Department of Energy Vehicle Battery R&D: Progress Update, https://www.hydrogen.energy.gov/pdfs/htac_nov2011_howell.pdf, (2011).
21. A. Manthiram, J. C. Knight, S.-T. Myung, S.-M. Oh and Y.-K. Sun, *Advanced Energy Materials*, 2016, **6**, 1501010.
22. K. M. Shaju, G. V. Subba Rao and B. V. R. Chowdari, *Electrochimica Acta*, 2002, **48**, 145-151.
23. I. Belharouak, W. Lu, D. Vissers and K. Amine, *Electrochemistry Communications*, 2006, **8**, 329-335.
24. J. Kim, H. Lee, H. Cha, M. Yoon, M. Park and J. Cho, *Advanced energy materials*, 2018, **8**, 1702028.
25. L. Ma, M. Nie, J. Xia and J. Dahn, *Journal of Power Sources*, 2016, **327**, 145-150.
26. T. Ohzuku, A. Ueda and M. Nagayama, *Journal of the Electrochemical Society*, 1993, **140**, 1862.
27. X. Zeng, G.-L. Xu, Y. Li, X. Luo, F. Maglia, C. Bauer, S. F. Lux, O. Paschos, S.-J. Kim, P. Lamp, J. Lu, K. Amine and Z. Chen, *ACS Applied Materials & Interfaces*, 2016, **8**, 3446-3451.
28. L. Zou, W. Zhao, Z. Liu, H. Jia, J. Zheng, G. Wang, Y. Yang, J.-G. Zhang and C. Wang, *ACS Energy*

- Letters*, 2018, **3**, 2433-2440.
29. H. Li, N. Zhang, J. Li and J. R. Dahn, *Journal of The Electrochemical Society*, 2018, **165**, A2985-A2993.
 30. S. S. Zhang, *InfoMat*, 2020, **2**, 942-949.
 31. A. Tomaszewska, Z. Chu, X. Feng, S. O'Kane, X. Liu, J. Chen, C. Ji, E. Endler, R. Li, L. Liu, Y. Li, S. Zheng, S. Vetterlein, M. Gao, J. Du, M. Parkes, M. Ouyang, M. Marinescu, G. Offer and B. Wu, *eTransportation*, 2019, **1**, 100011.
 32. S. S. Zhang, *ChemElectroChem*, 2020, **7**, 3569-3577.
 33. S. S. Zhang, *Energy Technology*, 2022, **n/a**, 2200370.
 34. A. Meintz, J. Zhang, R. Vijayagopal, C. Kreuzer, S. Ahmed, I. Bloom, A. Burnham, R. B. Carlson, F. Dias, E. J. Dufek, J. Francfort, K. Hardy, A. N. Jansen, M. Keyser, A. Markel, C. Michelbacher, M. Mohanpurkar, A. Pesaran, D. Scofield, M. Shirk, T. Stephens and T. Tanim, *Journal of Power Sources*, 201, **367**, 216-227.
 35. S. B. David Howell, Brian Cunningham, Samm Gillard, Lee Slezak, Enabling Fast Charging: A Technology Gap Assessment, https://www.energy.gov/sites/default/files/2017/10/f38/XFC%20Technology%20Gap%20Assessment%20Report_FINAL_10202017.pdf, (2017).
 36. M. Motors, i-MiEV charging features, <http://www.mitsubishicars.com/imiev/features/charging>, (accessed April, 2017).
 37. H. Boeriu, BMW and Nissan are joining forces to offer public DC Fast charging, <https://www.bmwblog.com/2015/12/21/bmw-and-nissan-are-joining-forces-to-offer-public-dc-fast-charging/>, (accessed December 21, 2015).
 38. B. USA, BMWi3: Overview, <https://www.bmwusa.com/vehicles/bmwi/i3.html>, (accessed April, 2017).
 39. Chevrolet, 2017 BOLT EV owner's manual, <https://my.chevrolet.com/content/dam/gmownercenter/gmna/dynamic/manuals/2017/Chevrolet/BOLT%20EV/Owner's%20Manual.pdf>, (accessed April, 2017).
 40. Tesla, Supercharger, <https://www.tesla.com/supercharger>, (accessed November 30, 2016).
 41. Tesla, Charging, <https://www.tesla.com/charging>, (accessed April, 2017).
 42. S. Ahmed, I. Bloom, A. N. Jansen, T. Tanim, E. J. Dufek, A. Pesaran, A. Burnham, R. B. Carlson, F. Dias, K. Hardy, M. Keyser, C. Kreuzer, A. Markel, A. Meintz, C. Michelbacher, M. Mohanpurkar, P. A. Nelson, D. C. Robertson, D. Scofield, M. Shirk, T. Stephens, R. Vijayagopal and J. Zhang, *Journal of Power Sources*, 2017, **367**, 250-262.
 43. J. Dahn, E. Fuller, M. Obrovac and U. Von Sacken, *Solid State Ionics*, 1994, **69**, 265-270.
 44. H. Arai, S. Okada, Y. Sakurai and J. i. Yamaki, *Journal of the Electrochemical Society*, 1997, **144**, 3117.
 45. R. Kostecky and F. McLarnon, *Electrochemical and solid-state letters*, 2004, **7**, A380.
 46. J. Dahn, U. von Sacken and C. Michal, *Solid State Ionics*, 1990, **44**, 87-97.
 47. I. Belharouak, W. Lu, D. Vissers and K. Amine, *Electrochemistry Communications*, 2006, **8**, 329-335.
 48. C. Delmas, J. Peres, A. Rougier, A. Demourgues, F. Weill, A. Chadwick, M. Broussely, F. Perton, P. Biensan and P. Willmann, *Journal of Power Sources*, 1997, **68**, 120-125.
 49. D. Caurant, N. Baffier, B. Garcia and J. Pereira-Ramos, *Solid State Ionics*, 1996, **91**, 45-54.
 50. A. Rougier, I. Saadoun, P. Gravereau, P. Willmann and C. Delmas, *Solid State Ionics*, 1996, **90**, 83-90.
 51. E. Rossen, C. Jones and J. Dahn, *Solid State Ionics*, 1992, **57**, 311-318.
 52. Y. Nitta, K. Okamura, K. Haraguchi, S. Kobayashi and A. Ohata, *Journal of power sources*, 1995, **54**, 511-515.

53. T. Ohzuku, A. Ueda and M. Kouguchi, *Journal of the Electrochemical Society*, 1995, **142**, 4033.
54. M. Guilnard, A. Rougier, M. Grüne, L. Croguennec and C. Delmas, *Journal of Power Sources*, 2003, **115**, 305-314.
55. Z. Liu, H. Zhen, Y. Kim and C. Liang, *Journal of Power Sources*, 2011, **196**, 10201-10206.
56. E. A. Olivetti, G. Ceder, G. G. Gaustad and X. Fu, *Joule*, 2017, **1**, 229-243.
57. D. Abraham, R. Twisten, M. Balasubramanian, J. Kropf, D. Fischer, J. McBreen, I. Petrov and K. Amine, *Journal of The Electrochemical Society*, 2003, **150**, A1450.
58. E. McCalla and J. Dahn, *Solid State Ionics*, 2013, **242**, 1-9.
59. S.-P. Lin, K.-Z. Fung, Y.-M. Hon and M.-H. Hon, *Journal of Solid State Chemistry*, 2002, **167**, 97-106.
60. H.-J. Noh, S. Youn, C. S. Yoon and Y.-K. Sun, *Journal of Power Sources*, 2013, **233**, 121-130.
61. X. Wang, Y. L. Ding, Y. P. Deng and Z. Chen, *Advanced Energy Materials*, 2020, **10**, 1903864.
62. A. Chen, K. Wang, J. Li, Q. Mao, Z. Xiao, D. Zhu, G. Wang, P. Liao, J. He, Y. You and Y. Xia, *Frontiers in Energy Research*, 2020, **8**.
63. S.-T. Myung, F. Maglia, K.-J. Park, C. S. Yoon, P. Lamp, S.-J. Kim and Y.-K. Sun, *ACS Energy Letters*, 2017, **2**, 196-223.
64. P. Yan, J. Zheng, T. Chen, L. Luo, Y. Jiang, K. Wang, M. Sui, J.-G. Zhang, S. Zhang and C. Wang, *Nature communications*, 2018, **9**, 1-8.
65. H.-H. Sun and A. Manthiram, *Chemistry of materials*, 2017, **29**, 8486-8493.
66. J. Zhang, C. Zheng, L. Li, Y. Xia, H. Huang, Y. Gan, C. Liang, X. He, X. Tao and W. Zhang, *Advanced Energy Materials*, 2020, **10**, 1903311.
67. H.-H. Ryu, K.-J. Park, C. S. Yoon and Y.-K. Sun, *Chemistry of Materials*, 2018, **30**, 1155-1163.
68. S. S. Zhang, *Journal of energy chemistry*, 2020, **41**, 135-141.
69. W. Li, J. Reimers and J. Dahn, *Solid State Ionics*, 1993, **67**, 123-130.
70. R. Jung, M. Metzger, F. Maglia, C. Stinner and H. A. Gasteiger, *Journal of The Electrochemical Society*, 2017, **164**, A1361.
71. C. S. Yoon, D.-W. Jun, S.-T. Myung and Y.-K. Sun, *ACS energy letters*, 2017, **2**, 1150-1155.
72. F. Kong, C. Liang, L. Wang, Y. Zheng, S. Peranathan, R. C. Longo, J. P. Ferraris, M. Kim and K. Cho, *Advanced Energy Materials*, 2019, **9**, 1802586.
73. Y. Wei, J. Zheng, S. Cui, X. Song, Y. Su, W. Deng, Z. Wu, X. Wang, W. Wang and M. Rao, *Journal of the American Chemical Society*, 2015, **137**, 8364-8367.
74. S. Cui, Y. Wei, T. Liu, W. Deng, Z. Hu, Y. Su, H. Li, M. Li, H. Guo, Y. Duan, W. Wang, M. Rao, J. Zheng, X. Wang and F. Pan, *Advanced Energy Materials*, 2016, **6**, 1501309.
75. K. Kang, Y. S. Meng, J. Breger, C. P. Grey and G. Ceder, *Science*, 2006, **311**, 977-980.
76. X. He, H. Sun, X. Ding and K. Zhao, *The Journal of Physical Chemistry C*, 2021, **125**, 10284-10294.
77. Y. Nomura, K. Yamamoto, Y. Yamagishi and E. Igaki, *Acs Nano*, 2021, **15**, 19806-19814.
78. G. T. Park, D. R. Yoon, U. H. Kim, B. Namkoong, J. Lee, M. M. Wang, A. C. Lee, X. W. Gu, W. C. Chueh, C. S. Yoon and Y. K. Sun, *Energy & Environmental Science*, 2021, **14**, 6616-6626.
79. C. Hong, Q. Leng, J. Zhu, S. Zheng, H. He, Y. Li, R. Liu, J. Wan and Y. Yang, *Journal of Materials Chemistry A*, 2020, **8**, 8540-8547.
80. J. C. Kim, D.-H. Seo, H. Chen and G. Ceder, *Advanced Energy Materials*, 2015, **5**, 1401916.
81. J. Lee, J. K. Papp, R. J. Clément, S. Sallis, D.-H. Kwon, T. Shi, W. Yang, B. D. McCloskey and G. Ceder, *Nature Communications*, 2017, **8**, 981.
82. K. Ku, S. B. Son, J. Gim, J. Park, Y. J. Liang, A. Stark, E. Lee and J. Libera, *Journal of Materials Chemistry A*, 2021, **10**, 288-295.

83. T. Y. Li, X. Z. Yuan, L. Zhang, D. T. Song, K. Y. Shi and C. Bock, *Electrochemical Energy Reviews*, 2020, **3**, 43-80.
84. C. Y. Mao, R. E. Ruther, J. L. Li, Z. J. Du and I. Belharouak, *Electrochemistry Communications*, 2018, **97**, 37-41.
85. E. Trevisanello, R. Ruess, G. Conforto, F. H. Richter and J. Janek, *Advanced Energy Materials*, 2021, **11**.
86. Z. Z. Yang, H. Charalambous, Y. L. Lin, S. E. Trask, L. Yu, J. G. Wen, A. Jansen, Y. F. Tsai, K. M. Wiaderek, Y. Ren and I. Bloom, *Journal of Power Sources*, 2022, **521**.
87. X. Y. Wu, B. H. Song, P. H. Chien, S. M. Everett, K. J. Zhao, J. Liu and Z. J. Du, *Advanced Science*, 2021, **8**.
88. Y. Yang, R. Xu, K. Zhang, S.-J. Lee, L. Mu, P. Liu, C. K. Waters, S. Spence, Z. Xu, C. Wei, D. J. Kautz, Q. Yuan, Y. Dong, Y.-S. Yu, X. Xiao, H.-K. Lee, P. Pianetta, P. Cloetens, J.-S. Lee, K. Zhao, F. Lin and Y. Liu, *Advanced Energy Materials*, 2019, **9**, 1900674.
89. J. Li, N. Sharma, Z. Jiang, Y. Yang, F. Monaco, Z. Xu, D. Hou, D. Ratner, P. Pianetta, P. Cloetens, F. Lin, K. Zhao and Y. Liu, *Science*, 2022, **376**, 517-521.
90. A. Mistry, F. L. E. Usseglio-Viretta, A. Colclasure, K. Smith and P. P. Mukherjee, *Journal of The Electrochemical Society*, 2020, **167**, 090542.
91. J. Park, H. Zhao, S. D. Kang, K. Lim, C.-C. Chen, Y.-S. Yu, R. D. Braatz, D. A. Shapiro, J. Hong, M. F. Toney, M. Z. Bazant and W. C. Chueh, *Nature Materials*, 2021, **20**, 991-999.
92. W. E. Gent, Y. Li, S. Ahn, J. Lim, Y. Liu, A. M. Wise, C. B. Gopal, D. N. Mueller, R. Davis, J. N. Weker, J.-H. Park, S.-K. Doo and W. C. Chueh, *Advanced Materials*, 2016, **28**, 6631-6638.
93. Z. Xu, Z. Jiang, C. Kuai, R. Xu, C. Qin, Y. Zhang, M. M. Rahman, C. Wei, D. Nordlund, C.-J. Sun, X. Xiao, X.-W. Du, K. Zhao, P. Yan, Y. Liu and F. Lin, *Nature Communications*, 2020, **11**, 83.
94. S. Xia, L. Mu, Z. Xu, J. Wang, C. Wei, L. Liu, P. Pianetta, K. Zhao, X. Yu, F. Lin and Y. Liu, *Nano Energy*, 2018, **53**, 753-762.
95. P. Yan, J. Zheng, M. Gu, J. Xiao, J.-G. Zhang and C.-M. Wang, *Nature Communications*, 2017, **8**, 14101.
96. R. Ruess, S. Schweidler, H. Hemmelmann, G. Conforto, A. Bielefeld, D. A. Weber, J. Sann, M. T. Elm and J. Janek, *Journal of The Electrochemical Society*, 2020, **167**, 100532.
97. R. Xu and K. Zhao, *Journal of the Mechanics and Physics of Solids*, 2018, **121**, 258-280.
98. Z. Jiang, J. Li, Y. Yang, L. Mu, C. Wei, X. Yu, P. Pianetta, K. Zhao, P. Cloetens, F. Lin and Y. Liu, *Nature Communications*, 2020, **11**, 2310.
99. H. Zhang, H. Liu, L. F. Piper, M. S. Whittingham and G. Zhou, *Chemical Reviews*, 2022, **122**, 5641-5681.
100. F. La Mantia, F. Rosciano, N. Tran and P. Novák, *Journal of The Electrochemical Society*, 2009, **156**, A823.
101. F. La Mantia, F. Rosciano, N. Tran and P. Novák, *Journal of Applied Electrochemistry*, 2008, **38**, 893-896.
102. J. Wandt, A. T. Freiberg, A. Ogrodnik and H. A. Gasteiger, *Materials Today*, 2018, **21**, 825-833.
103. A. O. Kondrakov, H. Geßwein, K. Galdina, L. de Biasi, V. Meded, E. O. Filatova, G. Schumacher, W. Wenzel, P. Hartmann, T. Brezesinski and J. Janek, *The Journal of Physical Chemistry C*, 2017, **121**, 24381-24388.
104. R. A. House, U. Maitra, L. Jin, J. G. Lozano, J. W. Somerville, N. H. Rees, A. J. Naylor, L. C. Duda, F. Massel, A. V. Chadwick, S. Ramos, D. M. Pickup, D. E. McNally, X. Lu, T. Schmitt, M. R. Roberts and P. G. Bruce, *Chemistry of Materials*, 2019, **31**, 3293-3300.

105. C. Wang, L. Han, R. Zhang, H. Cheng, L. Mu, K. Kisslinger, P. Zou, Y. Ren, P. Cao, F. Lin and H. L. Xin, *Matter*, 2021, **4**, 2013-2026.
106. L. Mu, R. Lin, R. Xu, L. Han, S. Xia, D. Sokaras, J. D. Steiner, T.-C. Weng, D. Nordlund, M. M. Doeff, Y. Liu, K. Zhao, H. L. Xin and F. Lin, *Nano Letters*, 2018, **18**, 3241-3249.
107. C. Liang, F. Kong, R. C. Longo, S. Kc, J.-S. Kim, S. Jeon, S. Choi and K. Cho, *The Journal of Physical Chemistry C*, 2016, **120**, 6383-6393.
108. R. Jung, M. Metzger, F. Maglia, C. Stinner and H. A. Gasteiger, *Journal of The Electrochemical Society*, 2017, **164**, A1361-A1377.
109. L. M. Morgan, M. M. Islam, H. Yang, K. O'Regan, A. N. Patel, A. Ghosh, E. Kendrick, M. Marinescu, G. J. Offer, B. J. Morgan, M. S. Islam, J. Edge and A. Walsh, *ACS Energy Letters*, 2022, **7**, 108-122.
110. R. Sahore, D. C. O'Hanlon, A. Tornheim, C.-W. Lee, J. C. Garcia, H. Iddir, M. Balasubramanian and I. Bloom, *Journal of The Electrochemical Society*, 2020, **167**, 020513.
111. J. Wandt, A. Freiberg, R. Thomas, Y. Gorlin, A. Siebel, R. Jung, H. A. Gasteiger and M. Tromp, *Journal of Materials Chemistry A*, 2016, **4**, 18300-18305.
112. J. A. Gilbert, I. A. Shkrob and D. P. Abraham, *Journal of The Electrochemical Society*, 2017, **164**, A389-A399.
113. D.-S. Ko, J.-H. Park, S. Park, Y. N. Ham, S. J. Ahn, J.-H. Park, H. N. Han, E. Lee, W. S. Jeon and C. Jung, *Nano Energy*, 2019, **56**, 434-442.
114. R. Jung, F. Linsenmann, R. Thomas, J. Wandt, S. Solchenbach, F. Maglia, C. Stinner, M. Tromp and H. A. Gasteiger, *Journal of The Electrochemical Society*, 2019, **166**, A378-A389.
115. Y. Liu, Y. Zhu and Y. Cui, *Nature Energy*, 2019, **4**, 540-550.
116. S. S. Zhang, *Energy Storage Materials*, 2020, **24**, 247-254.
117. F. Yang, Y. Liu, S. K. Martha, Z. Wu, J. C. Andrews, G. E. Ice, P. Pianetta and J. Nanda, *Nano Letters*, 2014, **14**, 4334-4341.
118. F. Lin, I. M. Markus, D. Nordlund, T.-C. Weng, M. D. Asta, H. L. Xin and M. M. Doeff, *Nature Communications*, 2014, **5**, 3529.
119. D. Mohanty, K. Dahlberg, D. M. King, L. A. David, A. S. Sefat, D. L. Wood, C. Daniel, S. Dhar, V. Mahajan, M. Lee and F. Albano, *Scientific Reports*, 2016, **6**, 26532.
120. J. Li, H. Li, W. Stone, R. Weber, S. Hy and J. R. Dahn, *Journal of The Electrochemical Society*, 2017, **164**, A3529-A3537.
121. H. Li, J. Li, X. Ma and J. R. Dahn, *Journal of The Electrochemical Society*, 2018, **165**, A1038-A1045.
122. J. Zhu and G. Chen, *Journal of Materials Chemistry A*, 2019, **7**, 5463-5474.
123. G. Qian, Y. Zhang, L. Li, R. Zhang, J. Xu, Z. Cheng, S. Xie, H. Wang, Q. Rao, Y. He, Y. Shen, L. Chen, M. Tang and Z.-F. Ma, *Energy Storage Materials*, 2020, **27**, 140-149.
124. Y. Lu, T. Zhu, E. McShane, B. D. McCloskey and G. Chen, *Small*, 2022, **18**, 2105833.
125. J. C. Garcia, J. Bareño, G. Chen, J. R. Croy and H. Iddir, *Physical Chemistry Chemical Physics*, 2020, **22**, 24490-24497.
126. S. Zhou, T. Mei, X. Wang and Y. Qian, *Nanoscale*, 2018, **10**, 17435-17455.
127. J. Tian, Y. Su, F. Wu, S. Xu, F. Chen, R. Chen, Q. Li, J. Li, F. Sun and S. Chen, *ACS Applied Materials & Interfaces*, 2016, **8**, 582-587.
128. A. van Bommel and J. R. Dahn, *Chemistry of Materials*, 2009, **21**, 1500-1503.
129. X. Zhang, W. J. Jiang, A. Mauger, Qilu, F. Gendron and C. M. Julien, *Journal of Power Sources*, 2010, **195**, 1292-1301.
130. N. Zhang, J. Li, H. Li, A. Liu, Q. Huang, L. Ma, Y. Li and J. R. Dahn, *Chemistry of Materials*, 2018, **30**,

- 8852-8860.
131. Y. Su, G. Chen, L. Chen, Y. Lu, Q. Zhang, Z. Lv, C. Li, L. Li, N. Liu, G. Tan, L. Bao, S. Chen and F. Wu, *ACS Applied Materials & Interfaces*, 2019, **11**, 36697-36704.
 132. Y. Lai, Z. Li, W. Zhao, X. Cheng, S. Xu, X. Yu and Y. Liu, *Nano Research*, 2020, **13**, 3347-3357.
 133. K. Yuan, N. Li, R. Ning, C. Shen, N. Hu, M. Bai, K. Zhang, Z. Tian, L. Shao, Z. Hu, X. Xu, T. Yu and K. Xie, *Nano Energy*, 2020, **78**, 105239.
 134. T. Weigel, F. Schipper, E. M. Erickson, F. A. Susai, B. Markovskiy and D. Aurbach, *ACS Energy Letters*, 2019, **4**, 508-516.
 135. F. Schipper, M. Dixit, D. Kovacheva, M. Talianker, O. Haik, J. Grinblat, E. M. Erickson, C. Ghanty, D. T. Major, B. Markovskiy and D. Aurbach, *Journal of Materials Chemistry A*, 2016, **4**, 16073-16084.
 136. K.-J. Park, H.-G. Jung, L.-Y. Kuo, P. Kaghazchi, C. S. Yoon and Y.-K. Sun, *Advanced Energy Materials*, 2018, **8**, 1801202.
 137. J. C. Kim, D.-H. Kwon, J. H. Yang, H. Kim, S.-H. Bo, L. Wu, H. Kim, D.-H. Seo, T. Shi, J. Wang, Y. Zhu and G. Ceder, *Advanced Energy Materials*, 2020, **10**, 2001151.
 138. P. Vassilaras, S. T. Dacek, H. Kim, T. T. Fister, S. Kim, G. Ceder and J. C. Kim, *Journal of The Electrochemical Society*, 2017, **164**, A3484.
 139. J. C. Kim, D.-H. Seo and G. Ceder, *Energy & Environmental Science*, 2015, **8**, 1790-1798.
 140. A. Gomez-Martin, F. Reissig, L. Frankenstein, M. Heidbüchel, M. Winter, T. Placke and R. Schmich, *Advanced Energy Materials*, 2022, **12**, 2103045.
 141. F. Xin, H. Zhou, X. Chen, M. Zuba, N. Chernova, G. Zhou and M. S. Whittingham, *ACS Applied Materials & Interfaces*, 2019, **11**, 34889-34894.
 142. P. Mohan and G. P. Kalaignan, *Journal of Electroceramics*, 2013, **31**, 210-217.
 143. P. Mohan, K. A. Kumar, G. P. Kalaignan and V. S. Muralidharan, *Journal of Solid State Electrochemistry*, 2012, **16**, 3695-3702.
 144. M. Eilers-Rethwisch, M. Winter and F. M. Schappacher, *Journal of Power Sources*, 2018, **387**, 101-107.
 145. L. Wu, X. Tang, X. Chen, Z. Rong, W. Dang, Y. Wang, X. Li, L. Huang and Y. Zhang, *Journal of Power Sources*, 2020, **445**, 227337.
 146. F. Schipper, H. Bouzaglo, M. Dixit, E. M. Erickson, T. Weigel, M. Talianker, J. Grinblat, L. Burstein, M. Schmidt, J. Lampert, C. Erk, B. Markovskiy, D. T. Major and D. Aurbach, *Advanced Energy Materials*, 2018, **8**, 1701682.
 147. G. Li, Z. Huang, Z. Zuo, Z. Zhang and H. Zhou, *Journal of Power Sources*, 2015, **281**, 69-76.
 148. H. H. Sun, A. Dolocan, J. A. Weeks, A. Heller and C. B. Mullins, *ACS Nano*, 2020, **14**, 17142-17150.
 149. G.-T. Park, B. Namkoong, S.-B. Kim, J. Liu, C. S. Yoon and Y.-K. Sun, *Nature Energy*, 2022, DOI: 10.1038/s41560-022-01106-6.
 150. U.-H. Kim, G.-T. Park, B.-K. Son, G. W. Nam, J. Liu, L.-Y. Kuo, P. Kaghazchi, C. S. Yoon and Y.-K. Sun, *Nature Energy*, 2020, **5**, 860-869.
 151. H.-H. Ryu, K.-J. Park, D. R. Yoon, A. Aishova, C. S. Yoon and Y.-K. Sun, *Advanced Energy Materials*, 2019, **9**, 1902698.
 152. H.-H. Ryu, N.-Y. Park, J. H. Seo, Y.-S. Yu, M. Sharma, R. Mücke, P. Kaghazchi, C. S. Yoon and Y.-K. Sun, *Materials Today*, 2020, **36**, 73-82.
 153. U.-H. Kim, J.-H. Park, A. Aishova, R. M. Ribas, R. S. Monteiro, K. J. Griffith, C. S. Yoon and Y.-K. Sun, *Advanced Energy Materials*, 2021, **11**, 2100884.
 154. J. U. Choi, N. Voronina, Y.-K. Sun and S.-T. Myung, *Advanced Energy Materials*, 2020, **10**, 2002027.
 155. S. J. Shi, J. P. Tu, Y. Y. Tang, Y. Q. Zhang, X. Y. Liu, X. L. Wang and C. D. Gu, *Journal of Power*

- Sources*, 2013, **225**, 338-346.
156. Z.-F. Tang, R. Wu, P.-F. Huang, Q.-S. Wang and C.-H. Chen, *Journal of Alloys and Compounds*, 2017, **693**, 1157-1163.
157. H. Yang, H.-H. Wu, M. Ge, L. Li, Y. Yuan, Q. Yao, J. Chen, L. Xia, J. Zheng, Z. Chen, J. Duan, K. Kisslinger, X. C. Zeng, W.-K. Lee, Q. Zhang and J. Lu, *Advanced Functional Materials*, 2019, **29**, 1808825.
158. Y. Chen, Y. Zhang, B. Chen, Z. Wang and C. Lu, *Journal of Power Sources*, 2014, **256**, 20-27.
159. S. Guo, B. Yuan, H. Zhao, D. Hua, Y. Shen, C. Sun, T. Chen, W. Sun, J. Wu, B. Zheng, W. Zhang, S. Li and F. Huo, *Nano Energy*, 2019, **58**, 673-679.
160. M. R. Laskar, D. H. K. Jackson, S. Xu, R. J. Hamers, D. Morgan and T. F. Kuech, *ACS Applied Materials & Interfaces*, 2017, **9**, 11231-11239.
161. S. Li, X. Fu, J. Zhou, Y. Han, P. Qi, X. Gao, X. Feng and B. Wang, *Journal of Materials Chemistry A*, 2016, **4**, 5823-5827.
162. Y. Zhang, C. S. Kim, H. W. Song, S.-J. Chang, H. Kim, J. Park, S. Hu, K. Zhao and S. Lee, *Energy Storage Materials*, 2022, **48**, 1-11.
163. M. Yoon, Y. Dong, J. Hwang, J. Sung, H. Cha, K. Ahn, Y. Huang, S. J. Kang, J. Li and J. Cho, *Nature Energy*, 2021, **6**, 362-371.
164. X. Li, J. Liu, M. N. Banis, A. Lushington, R. Li, M. Cai and X. Sun, *Energy & Environmental Science*, 2014, **7**, 768-778.
165. G.-L. Xu, Q. Liu, K. K. S. Lau, Y. Liu, X. Liu, H. Gao, X. Zhou, M. Zhuang, Y. Ren, J. Li, M. Shao, M. Ouyang, F. Pan, Z. Chen, K. Amine and G. Chen, *Nature Energy*, 2019, **4**, 484-494.
166. S. H. Lee, S. Yoon, E.-H. Hwang, Y.-G. Kwon, Y.-G. Lee and K. Y. Cho, *Journal of Power Sources*, 2018, **378**, 112-118.
167. P. Dong, D. Wang, Y. Yao, X. Li, Y. Zhang, J. Ru and T. Ren, *Journal of Power Sources*, 2017, **344**, 111-118.
168. Y. Liu, D. Sun, J. Zhou, Y. Qin, D. Wang and B. Guo, *ACS Applied Materials & Interfaces*, 2018, **10**, 11305-11310.
169. C. Wang, L. Yu, W. Fan, R. Liu, J. Liu, L. Ouyang, L. Yang and M. Zhu, *Journal of Alloys and Compounds*, 2018, **755**, 1-9.
170. B. Deng, H. Wang, X. Li, Y. Ding, D. Sun, J. Ma, M. Chen, T. Chen, F. Gao, M. Qu and G. Peng, *Energy Technology*, 2019, **7**, 1800981.
171. B. Deng, H. Wang, W. Ge, X. Li, X. Yan, T. Chen, M. Qu and G. Peng, *Electrochimica Acta*, 2017, **236**, 61-71.
172. S. Wang, S. Chen, W. Gao, L. Liu and S. Zhang, *Journal of Power Sources*, 2019, **423**, 90-97.
173. C.-G. Shi, C.-H. Shen, X.-X. Peng, C.-X. Luo, L.-F. Shen, W.-J. Sheng, J.-J. Fan, Q. Wang, S.-J. Zhang, B.-B. Xu, J.-J. Xian, Y.-M. Wei, L. Huang, J.-T. Li and S.-G. Sun, *Nano Energy*, 2019, **65**, 104084.
174. Q. Zheng, L. Xing, X. Yang, X. Li, C. Ye, K. Wang, Q. Huang and W. Li, *ACS Applied Materials & Interfaces*, 2018, **10**, 16843-16851.
175. Y. Zou, K. Zhou, G. Liu, N. Xu, X. Zhang, Y. Yang, J. Zhang and J. Zheng, *ACS Applied Materials & Interfaces*, 2021, **13**, 16427-16436.
176. T. Deng, X. Fan, L. Cao, J. Chen, S. Hou, X. Ji, L. Chen, S. Li, X. Zhou, E. Hu, D. Su, X.-Q. Yang and C. Wang, *Joule*, 2019, **3**, 2550-2564.
177. X. Y. Wang, S. Y. Li, W. D. Zhang, D. Wang, Z. Y. Shen, J. P. Zheng, H. L. L. Zhuang, Y. He and Y. Y. Lu, *Nano Energy*, 2021, **89**.

178. P. Bai, X. Ji, J. Zhang, W. Zhang, S. Hou, H. Su, M. Li, T. Deng, L. Cao, S. Liu, X. He, Y. Xu and C. Wang, *Angewandte Chemie International Edition*, 2022, **61**, e202202731.
179. W. D. Richards, L. J. Miara, Y. Wang, J. C. Kim and G. Ceder, *Chemistry of Materials*, 2016, **28**, 266-273.
180. K. Kim, H. Ma, S. Park and N.-S. Choi, *ACS Energy Letters*, 2020, **5**, 1537-1553.
181. M. Wood, J. Li, Z. Du, C. Daniel, A. R. Dunlop, B. J. Polzin, A. N. Jansen, G. K. Krumdick and D. L. Wood, *Journal of Power Sources*, 2021, **515**, 230429.
182. J. Hu, B. Wu, X. Cao, Y. Bi, S. Chae, C. Niu, B. Xiao, J. Tao, J. Zhang and J. Xiao, *Journal of Power Sources*, 2020, **454**, 227966.